Cell Reports

Article

Activation-induced chromatin reorganization in neurons depends on HDAC1 activity

Graphical abstract

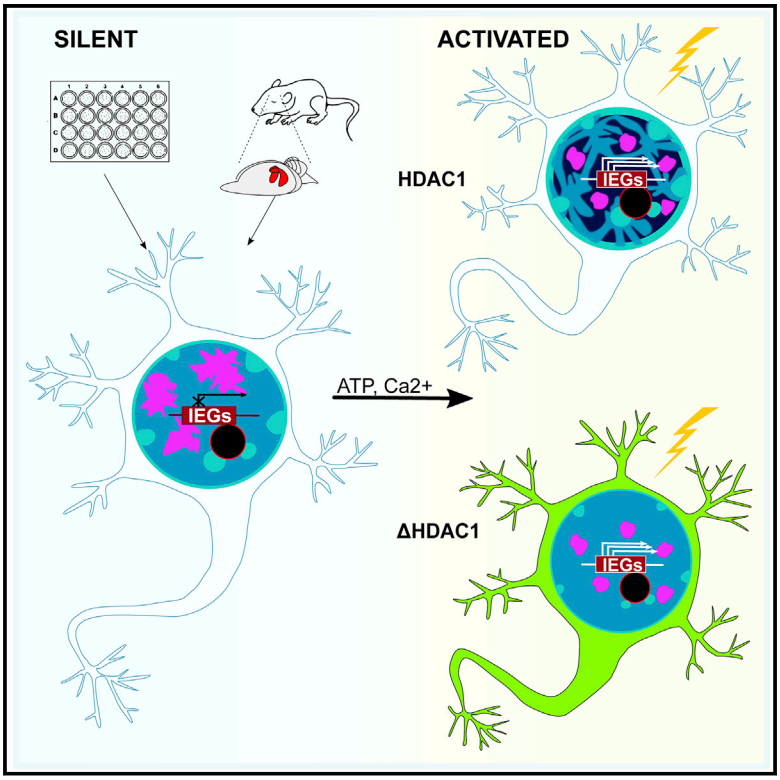

Highlights

- Stimulation of neurons induces condensation of large chromatin domains
- Chromatin condensation is an active, reversible, and energy- and calcium-dependent process
- Condensation is independent of transcription but fully relies on HDAC1 activity

Authors

Agnieszka Grabowska, Hanna Sas-Nowosielska, Bartosz Wojtas, ..., Dariusz Plewczynski, Grzegorz Marek Wilczynski, Adriana Magalska

Correspondence

a.magalska@nencki.edu.pl

In brief

Grabowska et al. show that neuronal cells respond to stimulation with condensation of large chromatin domains. This process is rapid, reversible, and energy-dependent. It is regulated by calcium-dependent signaling pathways and relies on the activity of HDAC1 histone deacetylase. It may constitute an important level of transcriptional regulation in neurons.

Grabowska et al., 2022, Cell Reports *38*, 110352
February 15, 2022 © 2022 The Author(s).
https://doi.org/10.1016/j.celrep.2022.110352

CellPress

Cell Reports

CellPress
OPEN ACCESS

Article

Activation-induced chromatin reorganization in neurons depends on HDAC1 activity

Agnieszka Grabowska,[1,13] Hanna Sas-Nowosielska,[1,13] Bartosz Wojtas,[3] Dagmara Holm-Kaczmarek,[1] Elzbieta Januszewicz,[2] Yana Yushkevich,[1] Iwona Czaban,[2] Pawel Trzaskoma,[2] Katarzyna Krawczyk,[2] Bartlomiej Gielniewski,[3] Ana Martin-Gonzalez,[2,4] Robert Kuba Filipkowski,[5] Krzysztof Hubert Olszynski,[5] Tytus Bernas,[6,7] Andrzej Antoni Szczepankiewicz,[2] Malgorzata Alicja Sliwinska,[6] Tambudzai Kanhema,[8,9] Clive R. Bramham,[8,9] Grzegorz Bokota,[10,11] Dariusz Plewczynski,[10,12] Grzegorz Marek Wilczynski,[2,14] and Adriana Magalska[1,15,*]

[1]Laboratory of Molecular Basis of Cell Motility, Nencki Institute of Experimental Biology, Polish Academy of Sciences, 02-093 Warsaw, Poland
[2]Laboratory of Molecular and Systemic Neuromorphology, Nencki Institute of Experimental Biology, Polish Academy of Sciences, 02-093 Warsaw, Poland
[3]Laboratory of Sequencing, Nencki Institute of Experimental Biology, Polish Academy of Sciences, 02-093 Warsaw, Poland
[4]Instituto de Neurociencias, Universidad Miguel Hernández-Consejo Superior de Investigaciones Científicas, San Juan de Alicante, 03550 Alicante, Spain
[5]Behavior and Metabolism Research Laboratory, Mossakowski Medical Research Institute, Polish Academy of Sciences, 02-106 Warsaw, Poland
[6]Laboratory of Imaging Tissue Structure and Function, Nencki Institute of Experimental Biology, Polish Academy of Sciences, 02-093 Warsaw, Poland
[7]Department of Anatomy and Neurology, VCU School of Medicine, Richmond, VA 23284, USA
[8]Department of Biomedicine, University of Bergen, 5020 Bergen, Norway
[9]KG Jebsen Centre for Neuropsychiatric Disorders, University of Bergen, 5020 Bergen, Norway
[10]Centre of New Technologies, University of Warsaw, 02-097 Warsaw, Poland
[11]Institute of Informatics, University of Warsaw, 02-097 Warsaw, Poland
[12]Faculty of Mathematics and Information Science, Warsaw University of Technology, 00-662 Warsaw, Poland
[13]These authors contributed equally
[14]Deceased on 13th of July, 2020
[15]Lead contact
*Correspondence: a.magalska@nencki.edu.pl
https://doi.org/10.1016/j.celrep.2022.110352

SUMMARY

Spatial chromatin organization is crucial for transcriptional regulation and might be particularly important in neurons since they dramatically change their transcriptome in response to external stimuli. We show that stimulation of neurons causes condensation of large chromatin domains. This phenomenon can be observed *in vitro* in cultured rat hippocampal neurons as well as *in vivo* in the amygdala and hippocampal neurons. Activity-induced chromatin condensation is an active, rapid, energy-dependent, and reversible process. It involves calcium-dependent pathways but is independent of active transcription. It is accompanied by the redistribution of posttranslational histone modifications and rearrangements in the spatial organization of chromosome territories. Moreover, it leads to the reorganization of nuclear speckles and active domains located in their proximity. Finally, we find that the histone deacetylase HDAC1 is the key regulator of this process. Our results suggest that HDAC1-dependent chromatin reorganization constitutes an important level of transcriptional regulation in neurons.

INTRODUCTION

In response to stimuli, neurons activate a transcriptional program essential for the transition from short- to long-term synaptic plasticity (Benito and Barco, 2015; Yap and Greenberg, 2018). This phenomenon is involved in cognitive functions, such as learning and memory, as well as in pathological disorders like epilepsy (Benito and Barco, 2015). Despite efforts aimed at investigating the underlying cellular and molecular pathways, regulation of transcriptional activation in neurons is still far from understood (Benito and Barco, 2015; Yap and Greenberg, 2018). One more recently discovered level of transcriptional regulation is the organization of chromatin in three-dimensional space over time (4D) (Finn and Misteli, 2019; Misteli, 2020). While most of these studies are focused on dividing cells, spatiotemporal chromatin organization could be particularly important in neurons, which are terminally differentiated and exhibit extensive transcriptome and epigenome changes in response to the external signals (Benito and Barco, 2015). Despite this presumption, the relationship between

This is an open access article under the CC BY-NC-ND license (http://creativecommons.org/licenses/by-nc-nd/4.0/).

genome organization and transcriptional activation remains largely unexplored in neurons.

Several studies over the years have reported specific changes to nuclear structure or organization as the result of neuronal activity. Barr and Bertram (1949, 1951) famously demonstrated that enhanced neuronal activity induces repositioning of the nucleolar satellite (formed most likely by the X chromosome and later called the Barr body) from the position adjacent to the nucleolus to the nuclear membrane. Later, Billia and colleagues (Billia et al., 1992) showed that long-term potentiation (LTP) was associated with the clustering of centromeric satellite DNA in the cell nuclei of rat acute brain slices. More recently, using organotypic hippocampal culture and electron microscopy, Tao-Cheng (2018) showed the clustering of chromatin within the nucleus of neurons subjected to membrane depolarization. Finally, our previous study indicated that perturbation of higher-order chromatin organization causes highly specific transcriptional defects in mouse pyramidal neurons and is accompanied by behavioral abnormalities (Ito et al., 2014). These findings demonstrate the link between specific structural rearrangements to the nuclear chromatin and neuronal activity; however, the mechanism underlying chromatin reorganization remains unknown.

4D chromatin organization is of particular interest when it comes to determining the mechanisms regulating neuronal activation. Indeed, the development of the chromosome conformation capture (3C)-based techniques has enabled more detailed insight into the changes in neuronal chromatin organization upon activation. These methods have revealed changes in the architecture of chromatin domains, manifested by the formation of new interactions between regulatory elements (Beagan et al., 2020; Lu et al., 2020). However, 3C-based data do not completely explain the earlier microscopic observations of large chromatin domains, such as Barr bodies or centromeres, that relocate in a response to stimulation (Barr and Bertram, 1951; Billia et al., 1992; Tao-Cheng, 2018). Furthermore, we and others (Finn et al., 2019; Trzaskoma et al., 2020) recently showed that population-based, 3C-related methods do not completely resolve chromatin organization at the single-cell level. Thus, in our present study, we turn to confocal, super-resolution, and electron microscopic methods to reveal information about the chromatin state at the single-cell level.

Using a variety of microscopic techniques coupled with quantitative image analysis and supported by RNA sequencing (RNA-seq) data, we show how stimulus-induced transcriptional activation affects both the chromatin organization in single neuronal cells and the global transcriptional state in neuronal cell populations. These approaches combined with a number of pharmacological and genetic perturbations provide insight into the behavior of different chromatin domains in activated neurons. Furthermore, we find that the mechanism underlying the transcriptional changes and structural rearrangements to chromatin upon neuronal stimulation requires the activity of the histone deacetylase HDAC1. We thus speculate that HDAC1-dependent reorganization of the chromatin enables the efficient transcription of thousands of genes involved in neuronal plasticity.

RESULTS

Chromatin organization undergoes significant rearrangement upon neuronal stimulation both *in vitro* and *in vivo*

To study how neural stimulation might affect global chromatin organization, we chemically induced LTP (cLTP) in rat hippocampal cultures (Figure 1A). High-throughput sequencing of mRNA (RNA-seq) analysis allowed identification of 708 up-regulated and 223 down-regulated genes, compared with control. Among up-regulated genes were early and delayed immediate-early genes (IEGs) (Figure 1B), similar to what was shown for neurons upon tetrodotoxin (TTX) withdrawal (Saha et al., 2011). Gene ontology and Kyoto Encyclopedia of Genes and Genomes (KEGG) analysis (Figure 1C; Tables S1–S3) of the up-regulated transcripts identified many genes pivotal for learning, memory, and other brain-related functions. We also found that down-regulated genes are involved in axon guidance, circadian rhythm, maintenance of stem cell fate, and regulation of cell metabolism.

Strikingly, we found that, upon cLTP, the chromatin of neurons undergoes global structural reorganization. The process starts immediately after cLTP induction when small foci of condensed chromatin form (Figure 2A). As the time of stimulation increases, these spots enlarge, forming easily distinguishable domains of condensed chromatin both in the nuclear interior and under the nuclear membrane. Activation of neurons was validated by the expression of c-FOS (Figure 2A), a well-established marker of neural activity (Filipkowski et al., 2000, 2001; Kaczmarek and Chaudhuri, 1997; Saha et al., 2011; Savonenko et al., 1999). Based on DNA staining intensity, we performed quantitative 3D confocal image analysis. Automatic Otsu (multiple Otsu [MO]; Figure 2B) thresholding was used to divide the nuclear volume into seven classes corresponding to increasing levels of chromatin condensation (Figures 2B, S1A, and S1B). Moreover, we assessed the relative heterogeneity of chromatin distribution by calculating the coefficient of variation (CV) of the pixel brightness. Such quantification revealed a gradual decrease in the volume occupied by chromatin (combined classes 2–7) upon stimulation of neurons (Figures 2B and S1B). The simultaneous increase in the volume of a highly condensed chromatin (MO class 6 and 7) and growing CV of DNA staining suggest progressive condensation of chromatin induced by neuronal stimulation (Figure 2B). Interestingly, in the first hour of stimulation, we observed a significant increase in the volume occupied by the most decondensed chromatin (MO class 2; Figure 2B), which localized in the proximity of interchromatin space. However, its levels returned to the control at 2 h of stimulation. Changes in chromatin organization were also confirmed using Hoechst fluorescence lifetime as an indicator of the chromatin viscosity and thus its condensation state. Hoechst lifetime is lower in condensed than in relaxed chromatin environment (Spagnol and Dahl, 2016), as was shown for chromatin of activated versus control neurons (Figure 2C). Interestingly, activity-dependent reorganization of chromatin was reversible, as washing out cLTP-inducing compounds allowed for a slow relaxation of chromatin (Figure 2D).

We further confirmed our observations using YOYO-1 DNA dye, which, unlike Hoechst, does not show any sequence preference

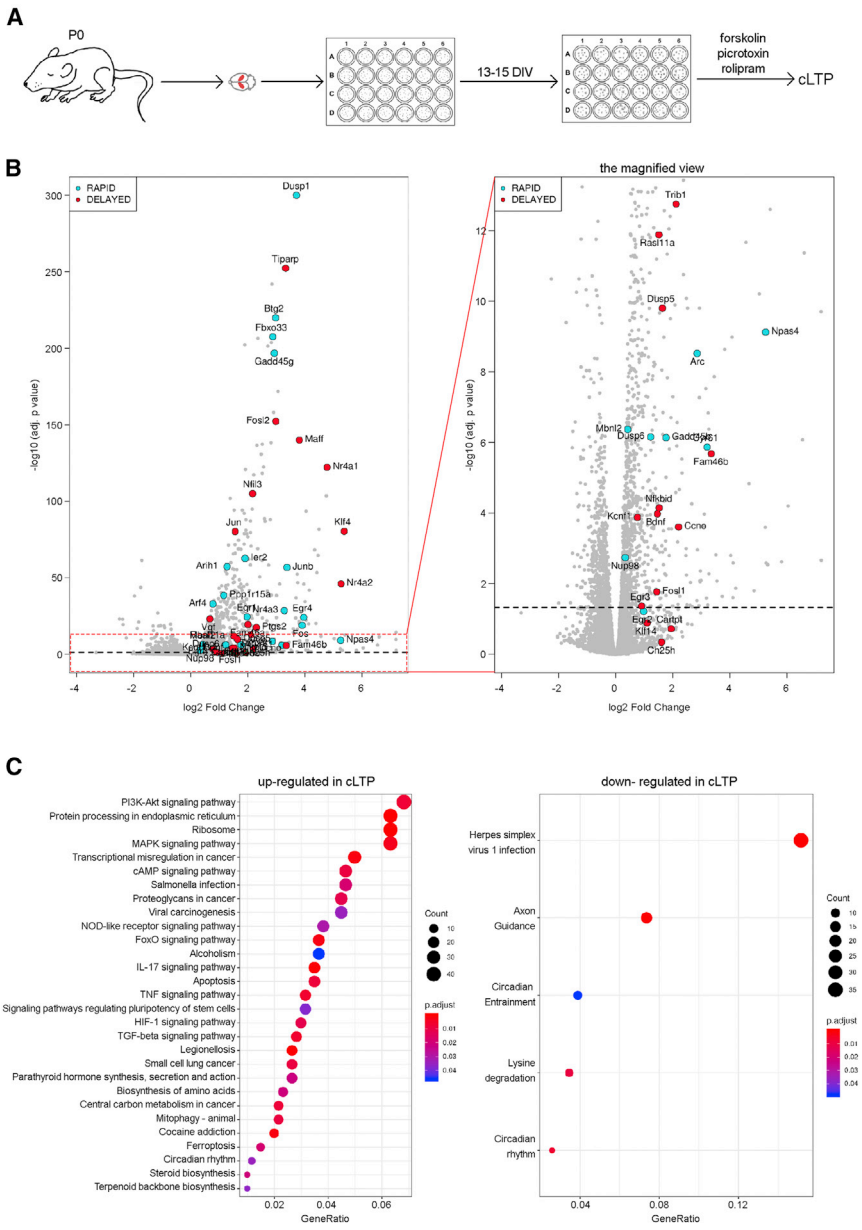

Figure 1. Confirmation of the experimental model

(A) Scheme of the experimental model.

(B) Volcano plot of RNA-seq results comparing gene expression in control and stimulated neurons. Rapid and delayed IEGs characterized as in Saha et al. (2011) are shown in red and blue, respectively. On the right, magnification of the genes with lower fold-change values is presented.

(C) KEGG pathways analysis of up- and down-regulated genes. The gene ratio was based on the number of identified activation-dependent up- or down-regulated genes and the number of genes involved in a given KEGG pathway. cAMP, cyclic AMP; MAPK, mitogen-activated protein kinase; NOD, non-obese diabetic; PI3K, phosphatidylinositol 3-kinase; TGF, transforming growth factor.

when binding DNA. After cLTP, we observed similar changes of both total and a highly condensed chromatin volume, as well as a CV of pixel intensity (Figure S1C). To exclude the possibility that the observed condensation was an outcome of cell death, we performed a viability test based on propidium iodide (PI) exclusion (Figure S1D). Furthermore, we imaged chromatin of activated neurons using super-resolution microscopy: structured illumination microscopy (SIM) (Figure 2E), stochastic optical reconstruction microscopy (STORM) (Figure 2F), and transmission electron microscopy (TEM) (Figure 2G). All techniques confirmed our previous observations: an apparent clustering of chromatin induced by neuronal stimulation accompanied by the increase of interchromatin space (Figures 2E–2G).

Changes in chromatin organization in the stimulated neurons occurred regardless of the stimulation method. We observed and quantified similar structural rearrangements of the chromatin in cultured neurons depolarized with potassium ions (KCl 2 h; Figures 3A and S2). These changes also occurred *in vivo* in activated pyramidal neurons of the amygdala of rats subjected to fear conditioning (FC) (2 h; Figures 3B and S2), granular neurons of the dentate gyrus of rats exposed to kainite-induced seizures (KA 2 h; Figures 3C and S2), or *in vivo* LTP induced by high-frequency stimulation (HFS) (1 h; Figures 3D and S2). Taken together, the observed global rearrangement of chromatin is part of a general physiological response of stimulated neuronal cells in both normal and pathological conditions.

Neuronal activation leads to changes in the distribution of active and silent chromatin

In the cell nucleus, chromosomes form chromosome territories (CTs). To get a more detailed view, we examined the structure of CTs of chromosomes 1 and 16, which differ in size, the number of genes, and also the content of constitutively silent chromatin (Vernole et al., 1984). Quantitative analysis of CTs visualized by DNA fluorescence *in situ* hybridization (DNA-FISH) showed that, after stimulation, the volume of CT 1 decreased, while its organization became more complex (Figure 4A). Conversely, the volume occupied by CT 16 increased (Figure 4B). Interestingly, the surface of both examined CTs expanded upon stimulation. To understand the reasons behind these discrepancies, we analyzed RNA-seq data in terms of the distribution of up- and down-regulated genes on individual chromosomes (Figures 4C, S3A, and S3B). It showed that chromosome 1 has fewer up-regulated

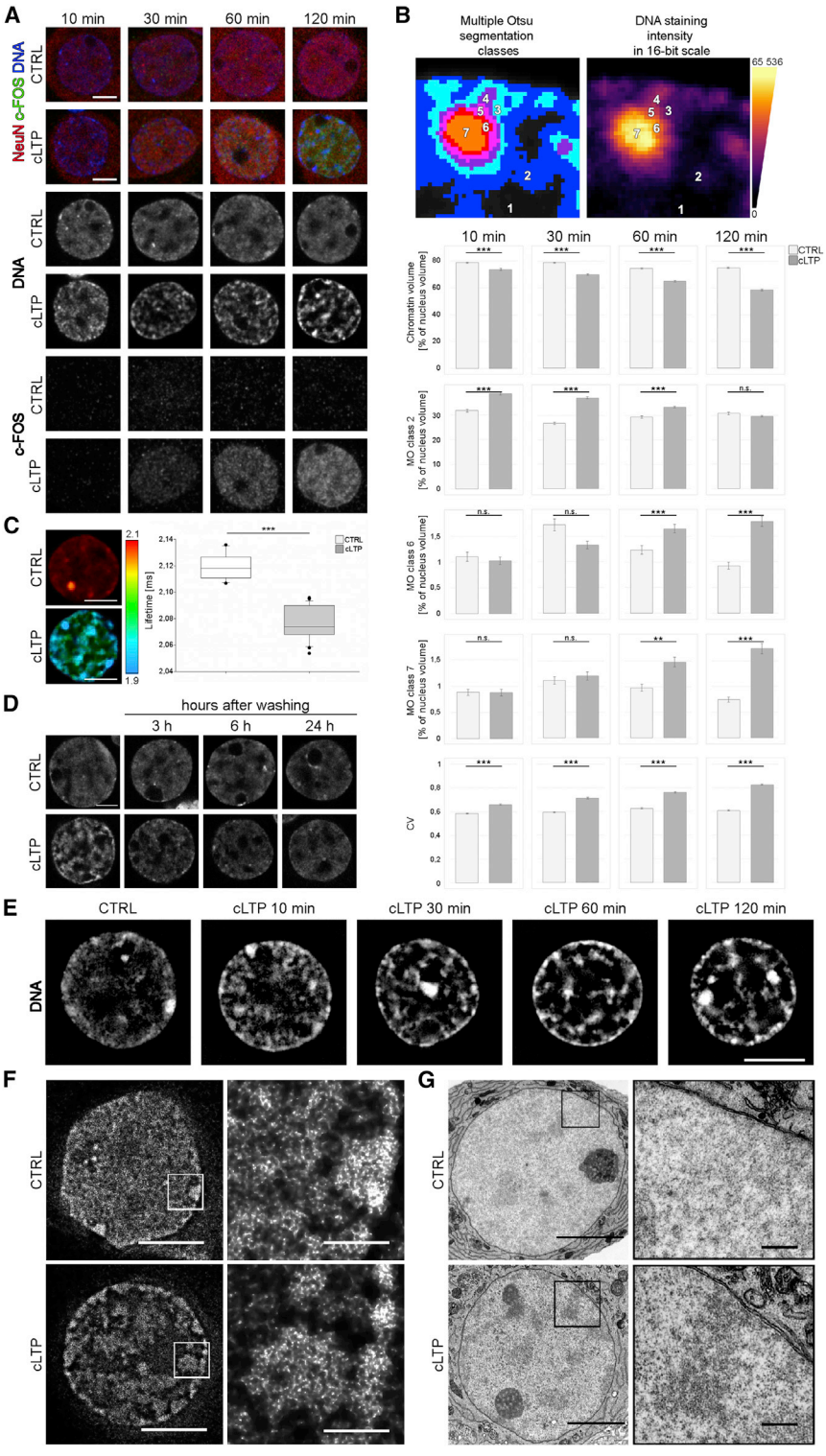

Figure 2. Condensation of the chromatin induced by LTP

(A) Time course of hippocampal neurons subjected to the chemically induced LTP (cLTP) and in control cells (CTRL). Panels show single confocal planes with NeuN neuronal marker (red), DNA (blue; gray in the middle panel), and c-FOS activity marker (green; gray in the lower panel).

(B) Example of multilevel Otsu's thresholding method, showing seven classes of chromatin with increasing DNA staining intensity (left panel). DNA staining in the color-coded scale is presented in the right panel. Histograms show quantification of the whole chromatin volume, the most decondensed (MO class 2), and highly condensed (MO classes 6 and 7) chromatin volume expressed as a percentage of nucleus volume made for analyzed time points. The CV represents the coefficient of variation of the pixel brightness of DNA staining. Results show average with SEM (n = 3); ***p < 0.001, **p < 0.01, and *p < 0.05 of the two-tailed, unpaired Mann-Whitney test.

(C) Mean fluorescence lifetime heatmaps of the Hoechst-stained DNA measured in CTRL and cLTP neuronal nuclei. Boxplot shows mean fluorescence lifetime calculated as in Spagnol and Dahl (2016). Results show average with SEM (n = 3); ***p < 0.001 of the two-tailed, unpaired Mann-Whitney test.

(D) Changes in chromatin condensation after cLTP-mixture wash out with a conditioned medium. Time course shows single confocal plains of chromatin in CTRL and cLTP neuron nuclei.

(E) Changes in chromatin organization visualized by SIM. Middle confocal plains of the time course of CRTL and cLTP neurons.

(F) Reconstruction of STORM images of chromatin of CTRL and cLTP neurons. On the right-side panels, the magnification of insets is shown.

(G) Chromatin of CTRL and cLTP neurons visualized with TEM microscopy. On the right-side panels, the magnification of insets is shown.

(A–G) Scale bars indicate 5 μm and 0.5 μm for magnification.

genes than is expected from its gene content (Figure S3A). However, the activity-up-regulated genes located on chromosome 1 showed significantly shorter distances between the neighboring gene's start sites than randomly selected genes, which suggest their clustering (Figure S3C). The necessity of exposure of a relatively modest amount of clustered genes to the transcriptionally permissive environment might explain the increase in the complexity of CT 1. Conversely, the portion of activated genes on chromosome 16 is proportional to the expected (Figure S3A), and the up-regulated genes are distributed along the whole length of the chromosome (Figures 4C and S3D); thus, the CT 16 expands more evenly. These results suggest that activity-induced reorganization of chromatin can lead to the redistribution of activated genes to a permissive chromatin environment localized at the periphery of CTs while maintaining the silenced genes in their core.

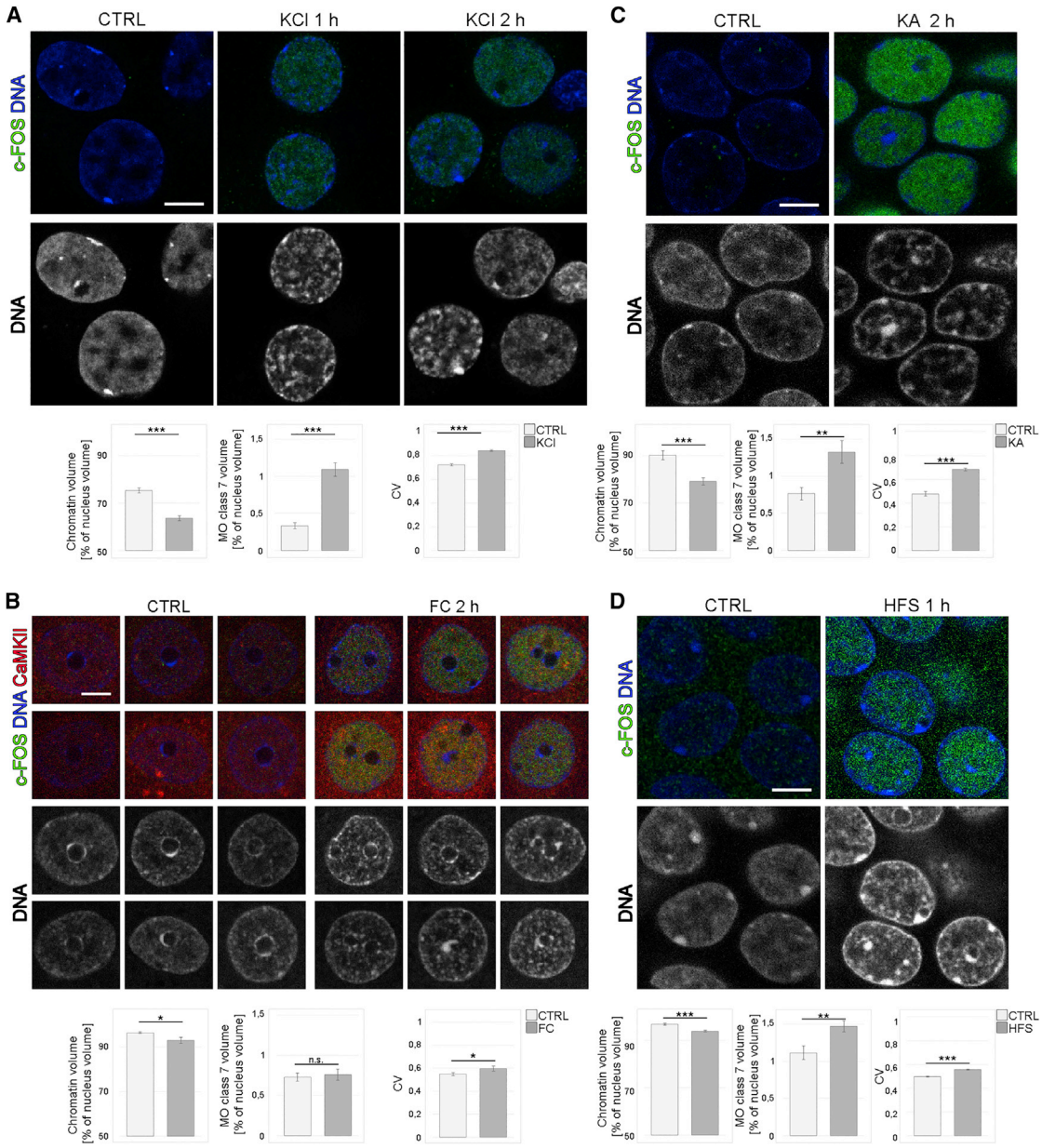

Figure 3. Condensation of the chromatin induced by different stimuli

(A) Nuclei of hippocampal neurons silenced with TTX and AP5 (CTRL), and activated with KCl for 1 or 2 h (KCl 1 h and 2 h).

(B) Confocal images (middle plain) of nuclei of the amygdala neurons of a control rat (CTRL) and animal subjected to a behavioral model of fear conditioning (FC 2 h). The marker of pyramidal neurons CaMKII is depicted in red.

(C) Neuronal nuclei from the dentate gyrus of hippocampal formation of a control rat (CTRL) and animal subjected to kainic-acid-induced seizures for 2 h (KA 2 h). Middle plain from confocal images is shown.

(D) Chromatin of neuronal nuclei after *in vivo* LTP in the dentate gyrus, induced by unilateral high-frequency stimulation (HFS 1 h) of the medial perforant path. The left panel shows chromatin in non-stimulated contralateral control (CTRL). (A–D) Expression of the c-FOS activity marker is depicted in green, and chromatin is shown in blue (gray on the lower panels).

Scale bars represent 5 μm. The quantitative analyses show average with SEM (n = 3); ***p < 0.001, **p < 0.01, and *p < 0.05 of the two-tailed, unpaired Mann-Whitney test.

As the transcriptional activity of chromatin is dependent on epigenetic marks, we decided to check the distribution of hetero- and euchromatin markers upon neuronal stimulation. The observed structural remodeling of chromatin was accompanied by changes in the localization of active and inactive chromatin. In control cells, markers of heterochromatin (Figures 5A and S4A) localized mainly to the most condensed chromatin-like chromocenters (H3K9me2 and 3, Figure S4A; H4K20me2/3, Figure 5A)

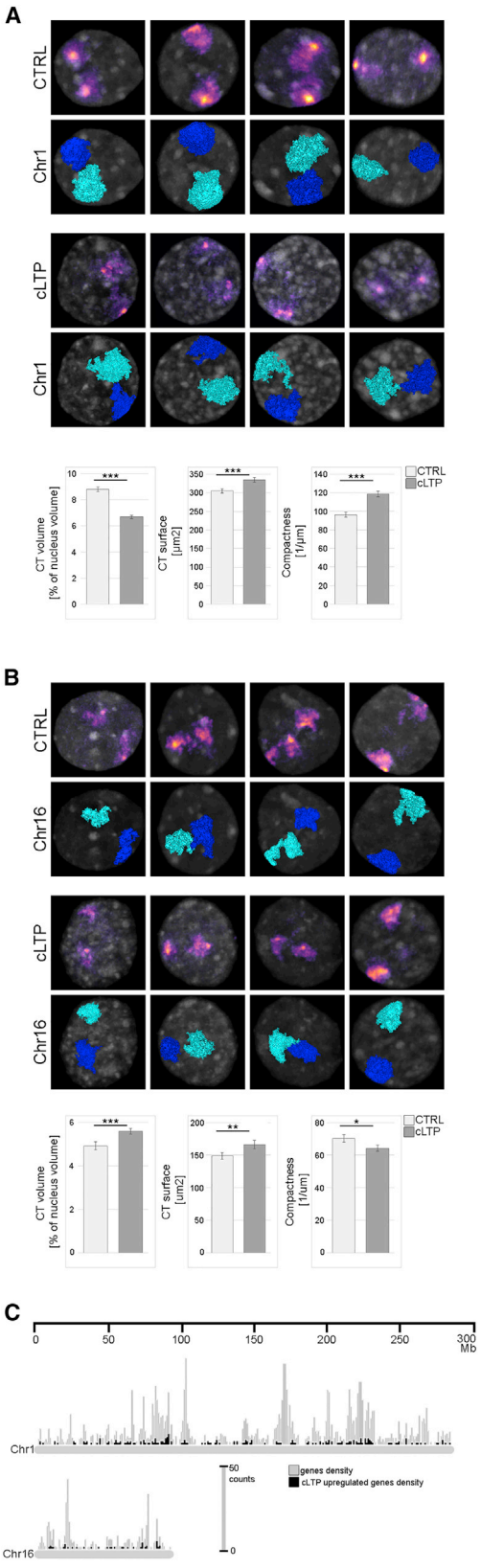

Figure 4. Chromosome territories' morphology changes upon neuronal stimulation

(A and B) 3D confocal images of control (CTRL) and stimulated (cLTP) neurons after FISH with a probe specific for rat chromosome 1 (pseudocolor in A) and chromosome 16 (pseudocolor in B). DNA staining (gray) and CT segmentations (lower panels of A and B) are shown. The quantitative analyses of the segmented CT show average with SEM (n = 3); ***$p < 0.001$, **$p < 0.01$, and *$p < 0.05$ of the two-tailed, unpaired Mann-Whitney test. CT volume is expressed as a percentage of nuclear volume.

(C) Gene density and abundance on chromosomes 1 and 16 are depicted in light gray. In black, the density and abundance of genes up-regulated by cLTP induction found in RNA-seq analysis are superimposed.

and Barr body (H3K27me3 and heterochromatin protein 1 β [HP1β], Figure S4A; histone macro H2A, Figure 5A). Some heterochromatin marks were also dispersed throughout the whole nucleus, except for H3K27me3 (Figure S4A), which was visible only at the Barr body. After stimulation, heterochromatin marks coincided with condensed chromatin. However, their total level was similar to the control cells (Figures 5A and S4A).

Euchromatin marks (H3K9ac and H3K4me3: Figures 5B and S4B) were present throughout the nucleus of control neurons, except for chromocenters. After stimulation, these histone marks accumulated close to the borders of condensed chromatin, around cores of dense heterochromatin foci. Interestingly, H3K4me3 mark did not coincide with H3K9ac and was localized most closely to the interchromatin space (Figures 5B and S4B). In addition, co-staining against the nuclear speckle's protein SF3a66 showed that H3K4me3 was enriched on the chromatin localized in the proximity to splicing speckles in control and stimulated neurons (Figure 5C). Quantitative analysis showed that, in stimulated neurons, speckles were more numerous and smaller than in control cells. However, the total volume of speckles did not change (Figure 5D). These results further support our notion that, in activated neurons, euchromatin becomes exposed to the interchromatin space where transcription and transcript processing takes place. The active compartment apparently surrounds transcriptionally silent, condensed parts of the genome.

Chromatin condensation does not depend on transcription or liquid-liquid phase separation but relies on the calcium-signaling pathway and requires energy supply

To determine whether stimulation-induced chromosome rearrangements are a cause or a consequence of transcriptional activation, we checked whether the global chromatin condensation depends on the transcription. To this end, we implemented two inhibitors: 5,6-dichloro-1-beta-D-ribofuranosylbenzimidazole (DRB) (Figures 6A and 6B) and α-amanitin (Figure 6B), which block transcription in distinct ways (Bensaude, 2011). Transcriptional inhibition was confirmed by ethynyl uridine (EU) incorporation assay (Figure 6A) and by verification of the c-FOS expression (Figure 6B; note also the disintegration of the nucleolus). Interestingly, the total RNA signal (EU staining) in stimulated neurons was weaker than in control cells and clustered in the interchromatin space (Figure 6A). Nonetheless, neither of the transcription inhibitors blocked the activity-dependent chromatin condensation (Figures 6B, 6C, S5A, and S5F). These results suggest that activity-dependent chromatin condensation is independent of active transcription.

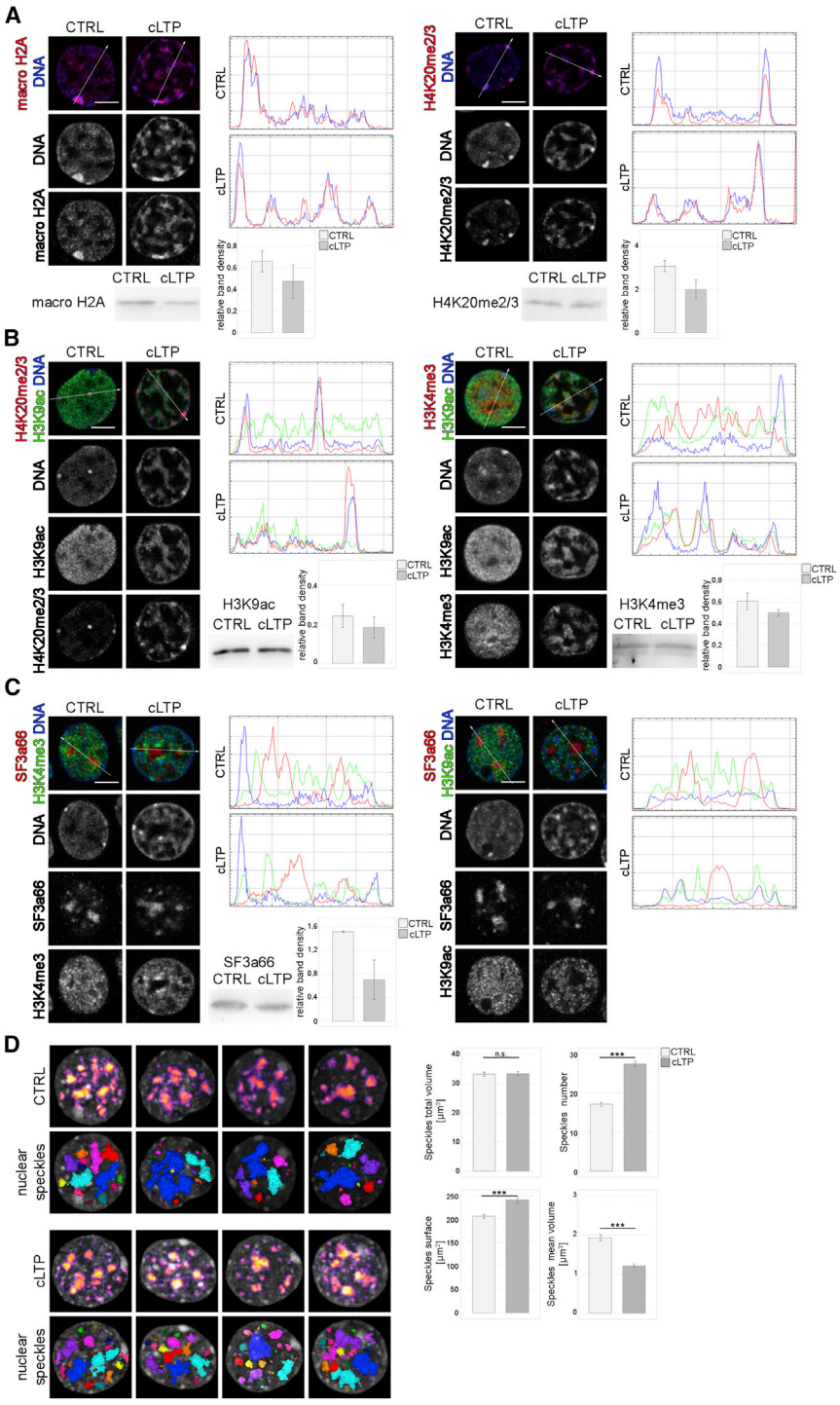

Figure 5. Silent and active chromatin distribution in control and stimulated hippocampal neurons

(A) Chromatin immunostained against the heterochromatin markers (red) and counterstained DNA (blue) of control (CTRL) and stimulated (cLTP) neurons. Scale bar represents 5 μm.

(B) Immunostaining of euchromatin (H3K9ac shown in green and H3K4me3 shown in red) and heterochromatin (H4K20me2/3 shown in red) markers of CTRL and cLTP neurons. DNA is shown in blue. Scale bar represents 5 μm.

(C) Immunostaining of nuclear speckles (red) and euchromatin markers (green) in CTRL and cLTP neurons. (A–C) RGB profiles show signal intensity values (0–255 range in the y axis) across arrows depicted on the merged images. At the bottom, western blot data and quantitative densitometric measurements for each antibody are shown. The histograms show average with SEM (n = 3). No significant changes were detected by the two-way ANOVA test. Scale bars represent 5 μm.

(D) 3D confocal images of nuclei of CTRL and cLTP neurons after immunostaining against nuclear speckles marker (SF3a66, in pseudocolor) and DNA staining (gray). Speckle segmentation is presented on the lower panels. The quantitative analyses show average with SEM (n = 3); ***p < 0.001, **p < 0.01, and *p < 0.05 of the two-tailed, unpaired Mann-Whitney test.

As there is increasing evidence for the role of liquid-liquid phase separation (LLPS) in organizing chromatin within the cell nucleus (Erdel and Rippe, 2018; Strom et al., 2017), we checked whether this mechanism could be responsible for the compartmentalization of silent and active chromatin in stimulated neurons. We treated control and stimulated neurons with 1,6-hexanediol, which breaks weak hydrophobic bonds engaged in LLPS (Erdel and Rippe, 2018; Strom et al., 2017). Treatment with hexanediol induced disintegration of nuclear speckles, formed by LLPS (Sawyer et al., 2019; Figure 6D), but it had a limited impact on activity-dependent chromatin condensation (Figures 6D, S5B, and S5F).

Next, we decided to block the calcium signaling pathway, one of the key pathways in neuronal activation. To this end, we inhibited calcineurin, a calmodulin-dependent serine/threonine protein phosphatase, which regulates the expression of IEGs (Qiu and Ghosh, 2008). As induction of cLTP is downstream of the calcium-dependent pathway, we turned to a more physiological stimulation mechanism—potassium ions. Inhibition of calcineurin by FK506 blocked transcription of *c-Fos* and hampered activity-dependent chromatin reorganization (Figures 6E, S5C, and S5F).

To determine whether activity-induced chromatin condensation is an ATP-dependent process, we pretreated neurons with oligomycin or iodoacetate, which reduces intracellular ATP levels (Hernández-Fonseca et al., 2008; Vian et al., 2018). Both treatments reduced ATP level by 90% (data not shown) and completely inhibited the c-FOS expression and activity-induced condensation of chromatin (Figures 6F, 6G, and S5D–S5F).

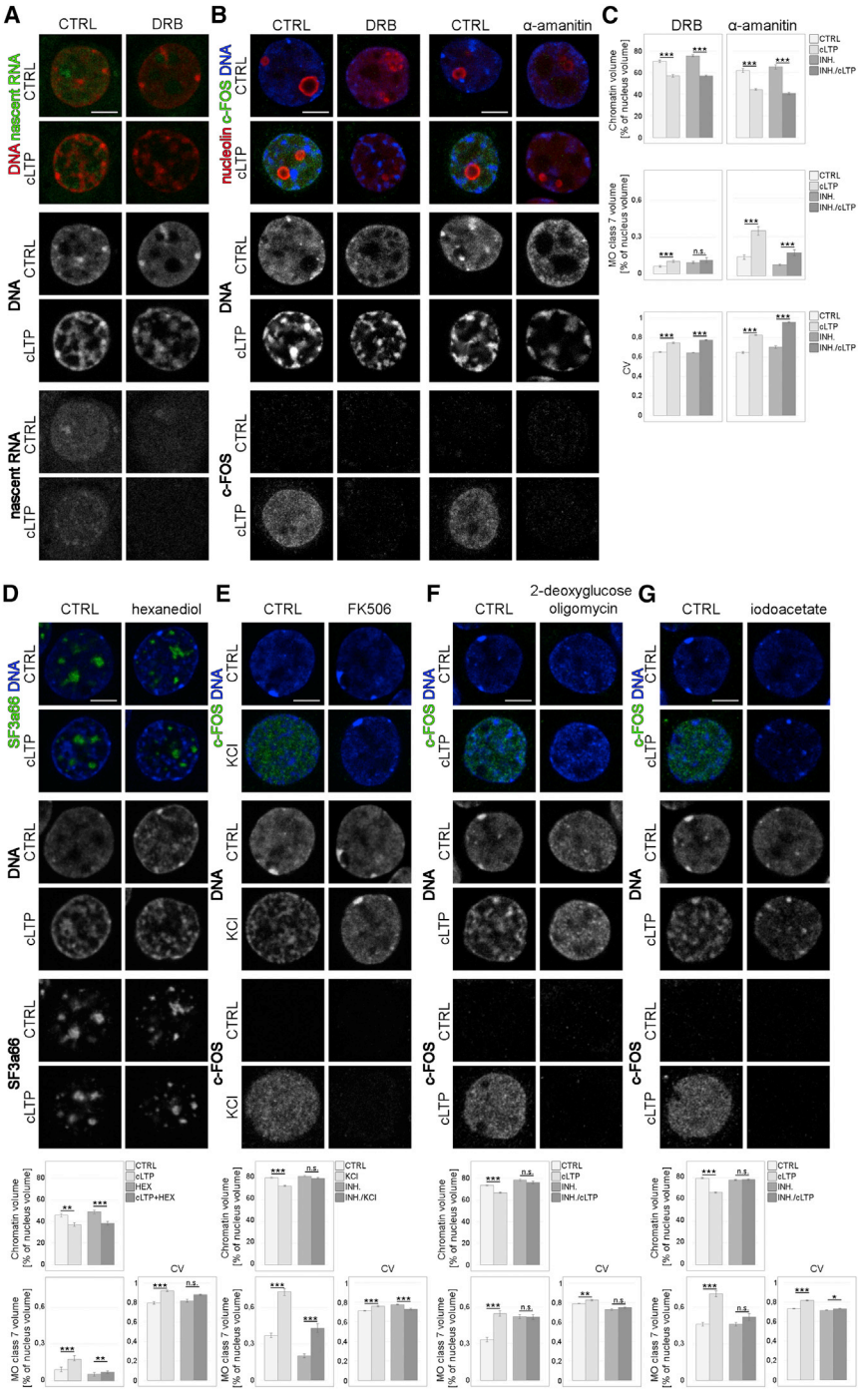

Figure 6. Chromatin condensation does not depend on the transcription or liquid-liquid phase separation, but relies on the calcium-signaling pathway and requires energy supply

(A–C) Confocal images of nuclei of control (CTRL) and stimulated (cLTP) neurons pretreated with DRB (A and B) or α-amanitin (B) transcription inhibitors.

(A) Nuclei after EU incorporation assay (newly synthesized RNA, green) and DNA (red) staining of CTRL and cLTP stimulated neurons are shown.

(B) Staining of c-FOS activity marker (green) and nucleolar marker- nucleolin (red) is shown.

(C) The quantitative analyses show average with SEM (n = 3); ***p < 0.001, **p < 0.01, and *p < 0.05 of the two-tailed, unpaired Kruskal-Wallis test.

(D) Chromatin in CTRL and cLTP neurons treated with 5% hexanediol (hexanediol) or vehicle. The DNA is shown in blue, and nuclear speckles (SF3a66) are shown in green.

(E) Hippocampal neurons silenced with TTX and AP5 (CTRL) and activated by KCl for 2 h (KCl), pretreated with calcineurin inhibitor (FK506). DNA staining is shown in blue, and immunostaining of c-FOS activity marker is depicted in green.

(F) and (G) Chromatin in CTRL and cLTP neurons, pretreated with 2-deoxyglucose and oligomycin (F) or sodium iodoacetate (G).

(A–G) show middle confocal plains of representative neuronal nuclei. Top panel shows merged images of single channels presented below. Scale bars represent 5 μm. The quantitative analyses show average with SEM (n = 3); ***p < 0.001, **p < 0.01, and *p < 0.05 of the two-tailed, unpaired Kruskal-Wallis test.

Thus, it seems that the reorganization of chromatin that occurs upon neuronal stimulation is an active process, which requires ATP, and it relies on calcium-dependent signaling.

Chromatin condensation upon neuronal activation is driven by HDAC1

To elucidate the mechanism underlying stimulation-induced chromatin condensation, we employed inhibitors, which block enzymes involved in reading, writing, or erasing histone modifications. None of the tested acetyltransferase and methyltransferase inhibitors blocked chromatin condensation or had an observable effect on the level of specific histone modifications in control or stimulated neurons (Figure S6). This might be due to the stability of epigenetic modifications and the fact that most chromatin modifiers fine-regulate epigenetic marks rather than affecting them globally. The tested JQ1 (Figure S6B) inhibitor, which disrupts super-enhancers (SEs) (Joo et al., 2015) had also no effect on chromatin condensation, which suggests that chromatin rearrangement induced by neuronal activation does not depend on SE-mediated regulation.

In contrast to the aforementioned inhibitors, pan-inhibitor of histone deacetylases, trichostatin A (TSA), completely blocked chromatin condensation with no effect on c-FOS expression (Figure S6E). To specify which histone deacetylase might regulate chromatin condensation, we used several histone deacetylase (HDAC) inhibitors with different target specificity (Figure S6F–S6H). All these inhibitors increased c-FOS expression

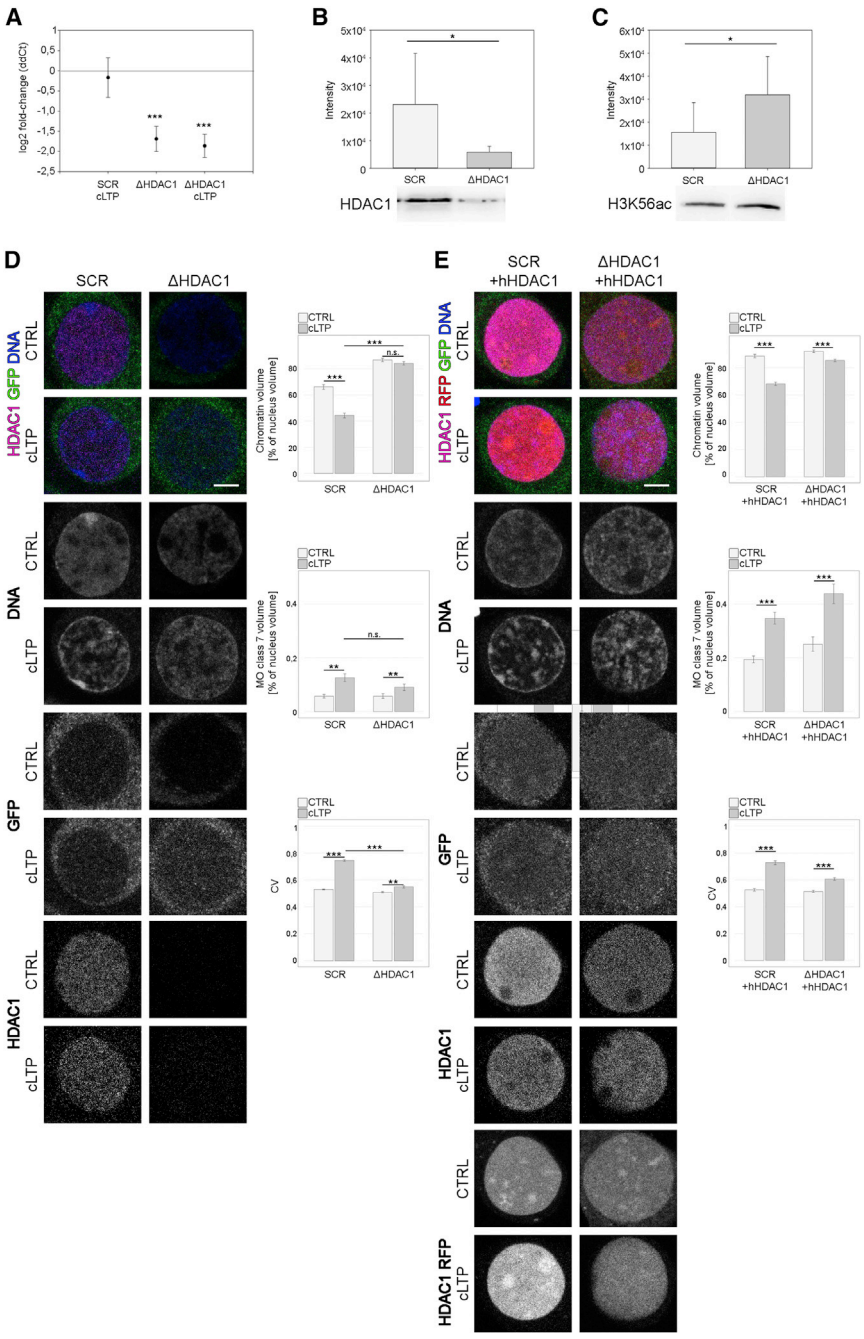

Figure 7. Activity-driven chromatin condensation depends on HDAC1

(A) RT-PCR analysis of HDAC1 transcript levels in control CTRL and stimulated (cLTP) hippocampal neurons transduced with GFP-expressing lentivirus (green) bearing scrambled control (SCR) or shRNA specific for HDAC1 (ΔHDAC1). The results normalized to control cells show average with SEM (n = 3); stars represent the two-way ANOVA test, where ***p < 0.001.

(B) and (C) Western blot analysis showing HDAC1 (B) and H3K56ac histone modification levels (C) in control (SCR) and HDAC1-depleted cells (ΔHDAC1). The histogram shows the average with SEM from a quantitative analysis of the bands' intensity (n = 3). Stars represent the two-way ANOVA test, where *p < 0.05.

(D) Immunostaining for HDAC1 (magenta) in control (CTRL) and stimulated (cLTP) neurons expressing GFP-tagged lentivirus (green) bearing scrambled control (SCR) or shRNA specific for HDAC1 (ΔHDAC1), counterstained to visualize DNA (blue).

(E) Nuclei of CTRL and cLTP neurons immunostained against HDAC1 (magenta). Cells transduced with GFP-tagged lentivirus (green) bearing scrambled control (SCR) or shRNA specific for rat HDAC1 (ΔHDAC1) and expressing human HDAC1 (hHDAC1, red) were counterstained to visualize DNA (blue).

In (D) and (E), single confocal plains of representative neuronal nuclei are shown. Scale bars represent 5 μm. The quantitative analyses show average with SEM (n = 3); ***p < 0.001, **p < 0.01, and *p < 0.05 of the two-tailed, unpaired Kruskal-Wallis test.

and histone H2B pan-acetylation. Based on their specific targets and the effect on chromatin condensation, we identified HDAC1 as a key regulator of neuronal-stimulation-induced chromatin reorganization.

To confirm the data from the HDAC inhibitor experiments, we depleted HDAC1 in neurons using short hairpin RNA (shRNA) (ΔHDAC1) (Figures 7A, 7B, 7D, and S7), which led to an increase in histone H3 acetylation at lysine 56, a specific HDAC1 target (Dovey et al., 2010; Figure 7C). As a control, we used scrambled (SCR) RNA without any known target in rat transcriptome. The chromatin of ΔHDAC1 neurons did not undergo condensation upon stimulation (Figures 7D and S7A). We could not see any change in chromatin volume in these cells (Figures 7D and S7B). Interestingly, similarly as in SCR controls, we could observe an increase in the volume occupied by the most condensed chromatin in ΔHDAC1 neurons (Figures 7D, S7A, and S7B). Nonetheless, chromatin reorganization analyzed with the CV of pixel brightness in control and stimulated cells showed much smaller differences in ΔHDAC1 cells than in SCR control (Figure 7D). In addition, HDAC1 depletion did not affect the reorganization of nuclear speckles induced by neuronal activation (Figure S7C). However, some differences in speckles number and volume between unstimulated SCR and ΔHDAC1 cells were present. HDAC1 silencing resulted in an increase in nuclear volume (Figure S7C), which might explain the expansion of both chromatin and interchromatin space in ΔHDAC1 cells (Figures 7D and S7B).

To ascertain that HDAC1 is a crucial regulator of chromatin condensation, we performed a rescue experiment using human HDAC1 (Figure 7E), which is not sensitive to rat-specific shRNA. The introduction of human HDAC1 restored the ability of

chromatin to condense (Figures 7E, S7A, and S7B). In rescued cells, the total volume of chromatin decreased, and there was an increase in the volume of condensed foci upon cLTP induction. Together, these results demonstrate a role for the histone deacetylase HDAC1 in activity-dependent chromatin reorganization in neurons.

DISCUSSION

Activity-dependent chromatin reorganization in neurons

Here, we show that the stimulation of neurons, both *in vitro* and *in vivo*, leads to a massive reorganization of chromatin, during which large chromatin domains become condensed. Since the early 1950s, evidence has been accumulating that particular chromatin domains are remodeled upon stimulation in neurons (Barr and Bertram, 1949, 1951; Billia et al., 1992; Tao-Cheng, 2018); however, no molecular mechanism of this phenomenon has been proposed to date.

Our results show that changes in the transcriptome of activated neurons are accompanied by global chromatin reorganization. How these two processes are interrelated remains unclear.

According to the current model proposed by Cremer et al. (2015), the cell nucleus is formed by two co-aligned domains—an active (ANC) and an inactive (INC) compartment. The ANC consists of an interchromatin compartment (IC) delineated by the perichromatin region (PR) formed by the chromatin loops of regulatory and coding sequences of actively transcribed genes. Available data allow modeling IC as a network of channel-like structures, mostly depleted of DNA, which starts at the nuclear pores and meanders the nuclear interior between chromatin domains (Cremer et al., 2015, 2020). Within the enlarged IC reside channels, splicing speckles, and other nuclear bodies. PR also embraces the INC formed by condensed chromatin clusters, in which permanently or temporarily transcriptionally silenced sequences reside (Masiello et al., 2018; Niedojadlo et al., 2011). It is tempting to speculate that chromatin reorganization upon activation of neurons could lead to a redistribution of subsequently activated, highly transcribed genes to the PR domain (Walczak et al., 2013), with a simultaneous retraction and condensation of silenced genes within the INC compartment. This is supported by our observation that the most decondensed chromatin domains, adjacent to interchromatin space, expand within the first minutes of neuronal stimulation, which is followed by a retraction of inactive chromatin into the most condensed compartment. This is also visible on the level of epigenetic marks where silent chromatin markers are present on the condensed chromatin and are separated from active markers, which reside in the proximity of nuclear speckles. Fernandez-Albert and colleagues (Fernandez-Albert et al., 2019) examined transcriptional and structural changes upon neuronal stimulation by kainic acid (KA), a glutamate receptor agonist, and by a novel context exploration. In line with our observations, they found a robust induction of enhancer RNAs and extra-coding RNAs, which was associated with a transient down-regulation of hundreds of transcripts, many of which are involved in basal metabolism and transcriptional regulation. The authors suggested that the activity-induced burst of gene expression transiently intercepts the transcriptional machinery. In our hands, KA and numerous other stimuli induced dramatic changes to chromatin morphology in hippocampal neurons *in vivo*, similarly to the remodeling caused by cLTP in the *in vitro* rat neuron model. Moreover, we observed a global reduction in the incorporation of EU in stimulated cells, with newly synthesized RNA mainly localized to the areas with very sparse or undetectable DNA staining.

3C-based techniques have revealed hundreds of *de novo* established interactions between promoters and enhancers (P-E), as well as the formation of the gene loops coupling transcription start sites (TSSs) and transcription termination sites (TTSs) of activity-induced genes in both *in vitro* (Beagan et al., 2020) and *in vivo* activation models (Fernandez-Albert et al., 2019). Beagan et al. (2020) found that 10% of loops surrounding IEGs, secondary response, and synaptic genes are induced by neuronal stimulation. However, it has been shown that most of the P-E interactions are established during neurogenesis and do not result in gene activation (Lu et al., 2020). Therefore, it seems likely that the gross morphological changes to chromatin structure visible in neurons upon stimulation are not reflected in chromatin interactions detected in genomics-based interaction datasets. Such a discrepancy may arise from the lower accessibility of condensed chromatin to restriction endonucleases used in 3C-based methods, which results in the detection of fewer contacts for these regions (Chandradoss et al., 2020). Moreover, biochemical methods based on ligation underestimate more complex contacts, involving multiple partners, which again will be more common in condensed chromatin domains (O'Sullivan et al., 2013). Only one recent study from Marco et al. (2020) supports our observation regarding large-scale chromatin reorganization. Using biochemical methods, including Hi-C and assay for transposase-accessible chromatin with high-throughput sequencing (ATAC-seq), the authors showed that memory formation leads to the relocalization of large chromatin segments with an average size of 436 kb between silenced and active chromatin compartments.

The activity-induced chromatin condensation in neurons may be another level of fine-tuning of transcriptional events in addition to the hierarchic expression of transcription factors, modification of histones, and chromatin looping. It has been shown that chromatin condensation leads to transcriptional silencing. Vaňková Hausnerová and Lanctôt (2017) demonstrated that, in the hypercondensed chromatin induced in conditions of high osmolarity, nascent transcription continues at a similar rate as in normal osmotic conditions. However, decondensation of chromatin was accompanied by a spike of transcription. Authors suggested that chromatin condensation leads to the accumulation of activated RNA polymerase II, which triggers the burst of transcription upon chromatin decondensation. However, our experiments with transcription inhibitors showed that stimulation-dependent chromatin condensation in neurons is independent of, and most probably precedes, the induction of transcriptional activity. Thus, we hypothesize that to facilitate the efficient transcription of thousands of genes involved in neuronal plasticity upon the activation of neuronal cells, ongoing transcription in other regions of the genome has to be reduced to the necessary minimum by chromatin condensation. This localized condensation, as well as the observed

fragmentation of nuclear speckles, leads to an increased contact area of the active chromatin and interchromatin space.

Global chromatin reorganization in stimulated neurons depends on histone deacetylases

It is generally accepted that gene activity is regulated by chromatin condensation, which in turn depends on certain histone marks (Bártová et al., 2008). The epigenetic state of chromatin is controlled by several groups of enzymes, among which HDACs are particularly important in neurons (Bártová et al., 2008; Kazantsev and Thompson, 2008; Volmar and Wahlestedt, 2015). Our results show that HDAC1 activity is crucial for the chromatin reorganization induced by neuronal activation. Both HDAC1 inhibitors and the depletion of HDAC1 led to the inhibition of chromatin condensation upon stimulation. There is a significant body of evidence pointing to the important role of HDACs in the regulation of gene expression in the brain (Van Dyke, 2014). Importantly, HDAC1 has been shown to play a role in the consolidation and extinction of fear memory (Siddiqui et al., 2019). Adler and Schmauss (2016) showed that decreasing association of HDAC1 with the promoters of plasticity-associated genes increased the expression of these genes and induced cognitive deficits triggered by early life stress. Similarly, the dissociation of HDAC1 from the promoters of specific IEGs in response to neuronal activation is necessary for their transcriptional activation (Qiu and Ghosh, 2008). Moreover, HDACs have also been implicated in the regulation of chromatin condensation in various models (Parker et al., 2007; Yamada et al., 2005).

Upon stimulation of neurons, the level of histone acetylation and other histone modifications was largely unchanged in our system. Following these observations, HDAC1 depletion did not result in any detectable change to histone modification levels aside from the increase of H3K56 acetylation. Thus, HDAC1 may be indirectly involved in activity-dependent chromatin condensation. Indeed, it has been shown that histones may not be the sole targets of HDAC activity. In response to HDAC's inhibitors, more than 1,700 proteins were found to be hyperacetylated, including transcription factors, chromatin remodelers, and protein kinases (Choudhary et al., 2009).

It has been shown that HDAC1 is bound to the CREST-BRG1 complex in unstimulated neurons, where it is responsible for transcriptional silencing of IEGs (Qiu and Ghosh, 2008). Upon stimulation, HDAC1 is released from the CREST-BRG1 complex by calcineurin phosphatase in a calcium-dependent manner, which in turn activates transcription. We demonstrated that the inhibition of calcineurin completely blocked chromatin reorganization upon the stimulation of neurons. It is tempting to speculate that HDAC1 might play a dual role in the observed chromatin reorganization. On the one hand, HDAC1 must be released from a portion of the genome to enable activity-dependent transcription (Qiu and Ghosh, 2008), and on the other hand, it is required, at the time of an activity-dependent burst of transcription, to induce the complete or partial silencing of certain genomic regions by promoting chromatin condensation. One of the possible HDAC1 targets are cohesins, as their activity is necessary for chromatin condensation (Makrantoni and Marston, 2018). Several lines of evidence connect deacetylases with cohesins (Borges et al., 2010; Jahnke et al., 2008; Thanh et al., 2020), a ring-like protein complex that can ultimately bring together two DNA segments from different locations. By a mechanism of ATP-dependent loop extrusion, cohesin promotes chromatin looping and plays a central role in the organization of the higher-order chromatin structure of mammalian genomes (Schwarzer et al., 2017). In our model, energy depletion blocked chromatin condensation induced by stimulation, which shows that condensation is also an active process relying on ATP. Thus, it is tempting to speculate that, in neurons, HDAC1 might induce chromatin condensation through a cohesin-dependent manner.

Here, we show that changes in chromatin organization occur *in vivo* in rats subjected to FC. Thus, HDAC1-dependent chromatin reorganization might be important for the formation of the structural memory of chromatin and, in consequence, one of the mechanisms involved in the formation of long-term memory. Indeed, our previous results in the rat model of epilepsy showed that changes in the spatial positioning of the Bdnf gene within the cell nucleus are induced by neuronal activation and are correlated with the level of its expression (Walczak et al., 2013). Importantly, the repositioning of the Bdnf alleles persisted for up to 4 weeks and correlated with a stronger mossy fiber sprouting, a pathological form of excitatory circuit formation typical in the development of epilepsy (Skupien-Jaroszek et al., 2021). We suggested that, despite the low level of BDNF expression 4 weeks after KA administration, the repositioned alleles may be associated with the poised RNA polymerase II, which would sensitize them for immediate transcription once the neuronal activation occurs. Here, we show additionally that chromatin condensation is preceded by the expansion of the active perichromatin region. The aforementioned publication of Marco et al. (2020) also seems to confirm this idea. The authors showed that memory encoding involving the activation of neurons leads to a general increase in chromatin accessibility without the expected change in gene expression. The later event of memory consolidation results in a spatial reorganization of large chromatin segments and P-E interactions, which are later used in memory recall to up-regulate genes involved in structural plasticity. Our data suggest that activity-driven chromatin condensation is a gradual process, whose strength and persistence are correlated with the duration of stimulation. This is supported by early works of Barr and Bertram (1949, 1951), which showed that 8 h of electrical stimulation of cat neurons led to the long-lasting repositioning of the Barr body, and in our hands, the stimulation of rats with KA resulted in a persistent repositioning of *Bdnf* (Skupien-Jaroszek et al., 2021; Walczak et al., 2013).

Together, these data suggest that activity-driven chromatin reorganization might lead to stable changes in chromatin organization, which conduct gene expression to facilitate the formation of neuronal circuits in physiological and pathological processes.

Limitations of the study

The presented results are based mainly on microscopy techniques. Although we can see a clear dependence between the activity-induced chromatin condensation in neurons and HDAC1 activity, we have not pinpointed the exact mechanism

underlying this process. Therefore, it would be interesting to investigate potential HDAC1 partners as well as HDAC1 enrichment on chromatin in silent and activated neurons. Although our results showed the increasing volume of the highly condensed chromatin domains upon neuronal stimulation, we did not show the sequence specificity and genomic features of these regions. Those condensed domains morphologically resemble chromocenters and seem to be continuous with them. Chromocenters are heterochromatic domains, built with pericentromeric chromatin and marked by H3K9me3, H4K20me3, and HP1 proteins, and heterochromatin has been shown to be able to actively spread on the surrounding chromatin. Thus, it is tempting to speculate that chromocenters might initiate the condensation of chromatin during neuronal activation.

STAR★METHODS

Detailed methods are provided in the online version of this paper and include the following:

- KEY RESOURCES TABLE
- RESOURCE AVAILABILITY
  - Lead contact
  - Materials availability
  - Data and code availability
- EXPERIMENTAL MODEL AND SUBJECT DETAILS
  - Animals
- METHOD DETAILS
  - Induction of seizures
  - Fear conditioning
  - *In vivo* LTP by High Frequency Stimulation
  - Cell culture
  - Chemical LTP
  - Stimulation with potassium chloride
  - RNA labeling/EU incorporation assay
  - Propidium iodide exclusion test
  - Washing out of the cLTP inducing mixture
  - HDAC1 silencing and Addback experiments
  - Treatments
  - Cloning
  - Western blotting
  - Immunodetection
  - Immunodetection on brain slices
  - 3D DNA-FISH
  - EM sample preparation
  - Transmission electron microscopy
  - Confocal microscopy
  - Fluorescence lifetime imaging
  - STochastic optical reconstruction microscopy (STORM)
  - Structure illumination microscopy (SIM)
  - Quantitative image analysis
  - RNA isolation
  - Transcriptomic analysis (RNA sequencing)
  - Enrichment of up/down-regulated genes
  - cLTP/CTRL up -regulated genes clustering
  - Quantitative RT-PCR
- QUANTIFICATION AND STATISTICAL ANALYSIS

SUPPLEMENTAL INFORMATION

Supplemental information can be found online at https://doi.org/10.1016/j.celrep.2022.110352.

ACKNOWLEDGMENTS

This work was supported by the National Science Centre grant nos. UMO-2015/18/E/NZ3/00730 (A.M., A.G., H.S.N., E.J. and Y.Y.), 2014/15/N/NZ2/00379 and 2017/24/T/NZ2/00307 (P.T.), 2019/35/O/ST6/02484 (D.P. and G.B.), and 2014/14/M/NZ4/00561 (K.H.O. and R.K.F.). B.W. and B.G. were supported by the Foundation for Polish Science TEAM-TECH Core Facility project "NGS platform for comprehensive diagnostics and personalized therapy in neuro-oncology," Foundation for Polish Science co-financed by the European Union under the European Regional Development Fund (TEAM to D.P.). A.M.G. was supported by the H2020-MSCA-COFUND-2014 grant Bio4-Med (GA no. 665735). We are grateful to Dr. Allana Schooley (University of Massachusetts Medical School) for critical reading of the manuscript and valuable discussion. We would also like to thank members of core facilities listed in STAR Methods for help and Dr. Piotr Michaluk for providing us with plasmids.

AUTHOR CONTRIBUTIONS

A.G. and H.S.-N. designed and performed most experiments; D.H.K. and T.B. designed and performed STORM imaging and processing; E.J. made KCl stimulation; Y.Y. made cell cultures; I.C. and A.A.S. performed kainite-induced seizures and tissue processing; Y.Y., P.T., and K.K. designed and made FISH experiments; B.W. and B.G. made RNA-seq libraries and analysis; A.M.-G., R.K.F., and K.H.O. made the fear conditioning experiment and brain-tissue processing; M.A.S. made TEM experiment; T.K. and C.R.B. made *in vivo* LTP; G.B. and D.P. developed image quantification strategies; G.M.W. initiated the project; A.M. and H.S.-N. wrote the manuscript; and A.M. designed and supervised the project. All authors contributed to commenting and editing the manuscript.

DECLARATION OF INTERESTS

The authors declare no competing interests.

Received: February 9, 2021
Revised: November 9, 2021
Accepted: January 19, 2022
Published: February 15, 2022

REFERENCES

Adler, S.M., and Schmauss, C. (2016). Cognitive deficits triggered by early life stress: the role of histone deacetylase 1. Neurobiol. Dis. *94*, 1–9.

Barr, M.L., and Bertram, E.G. (1949). A morphological distinction between neurones of the male and female, and the behaviour of the nucleolar satellite during accelerated nucleoprotein synthesis. Nature *163*, 676–677.

Barr, M.L., and Bertram, E.G. (1951). The behaviour of nuclear structures during depletion and restoration of Nissl material in motor neurons. J. Anat. *85*, 171–181.

Bártová, E., Krejčí, J., Harničarová, A., Galiová, G., and Kozubek, S. (2008). Histone modifications and nuclear architecture: a review. J. Histochem. Cytochem. *56*, 711–721.

Beagan, J.A., Pastuzyn, E.D., Fernandez, L.R., Guo, M.H., Feng, K., Titus, K.R., Chandrashekar, H., Shepherd, J.D., and Phillips-Cremins, J.E. (2020). Three-dimensional genome restructuring across timescales of activity-induced neuronal gene expression. Nat. Neurosci. *23*, 707–717.

Benito, E., and Barco, A. (2015). The neuronal activity-driven transcriptome. Mol. Neurobiol. *51*, 1071–1088.

Bensaude, O. (2011). Inhibiting eukaryotic transcription: which compound to choose? how to evaluate its activity? Transcription *2*, 103–108.

Billia, F., Baskys, A., Carlen, P.L., and De Boni, U. (1992). Rearrangement of centromeric satellite DNA in hippocampal neurons exhibiting long-term potentiation. Mol. Brain Res. *14*, 101–108.

Bokota, G., Sroka, J., Basu, S., Das, N., Trzaskoma, P., Yushkevich, Y., Grabowska, A., Magalska, A., and Plewczynski, D. (2021). PartSeg: a tool for quantitative feature extraction from 3D microscopy images for dummies. BMC Bioinformatics *22*, 72.

Borges, V., Lehane, C., Lopez-Serra, L., Flynn, H., Skehel, M., Ben-Shahar, T.R., and Uhlmann, F. (2010). Hos1 deacetylates Smc3 to close the cohesin acetylation cycle. Mol. Cell *39*, 677–688.

Chandradoss, K.R., Guthikonda, P.K., Kethavath, S., Dass, M., Singh, H., Nayak, R., Kurukuti, S., and Sandhu, K.S. (2020). Biased visibility in Hi-C datasets marks dynamically regulated condensed and decondensed chromatin states genome-wide. BMC Genomics *21*, 1–15.

Choudhary, C., Kumar, C., Gnad, F., Nielsen, M.L., Rehman, M., Walther, T.C., Olsen, J.V., and Mann, M. (2009). Lysine acetylation targets protein complexes and co-regulates major cellular functions. Science *325*, 834–840.

Cremer, M., Grasser, F., Lanctôt, C., Müller, S., Neusser, M., Zinner, R., Solovei, I., and Cremer, T. (2012). Multicolor 3D Fluorescence *in situ* hybridization for imaging interphase chromosomes *1*, 205–239.

Cremer, T., Cremer, M., Hübner, B., Strickfaden, H., Smeets, D., Popken, J., Sterr, M., Markaki, Y., Rippe, K., and Cremer, C. (2015). The 4D nucleome: evidence for a dynamic nuclear landscape based on co-aligned active and inactive nuclear compartments. FEBS Lett. *589*, 2931–2943.

Cremer, T., Cremer, M., Hübner, B., Silahtaroglu, A., Hendzel, M., Lanctôt, C., Strickfaden, H., and Cremer, C. (2020). The interchromatin compartment participates in the structural and functional organization of the cell nucleus. BioEssays *42*, 1–18.

Deerinck, T.J., Bushong, E.A., Thor, A., and Ellisman, M.H. (2010). NCMIR methods for 3D EM: a new protocol for preparation of biological specimens for serial block face scanning electron microscopy. Microscopy, 6–8.

Dobin, A., Davis, C.A., Schlesinger, F., Drenkow, J., Zaleski, C., Jha, S., Batut, P., Chaisson, M., and Gingeras, T.R. (2013). STAR: ultrafast universal RNA-seq aligner. Bioinformatics *29*, 15–21.

Dovey, O.M., Foster, C.T., and Cowley, S.M. (2010). Histone deacetylase 1 (HDAC1), but not HDAC2, controls embryonic stem cell differentiation. Proc. Natl. Acad. Sci. U. S. A. *107*, 8242–8247.

Van Dyke, M.W. (2014). Lysine deacetylase (KDAC) regulatory pathways: an alternative approach to selective modulation. ChemMedChem *9*, 511–522.

Emiliani, S., Fischle, W., Van Lint, C., Al-Abed, Y., and Verdin, E. (1998). Characterization of a human RPD3 ortholog Hdac3. Proc. Natl. Acad. Sci. U S A *95*, 2795–2800.

Erdel, F., and Rippe, K. (2018). Formation of chromatin subcompartments by phase separation. Biophys. J. *114*, 2262–2270.

Fernandez-Albert, J., Lipinski, M., Lopez-Cascales, M.T., Rowley, M.J., Martin-Gonzalez, A.M., del Blanco, B., Corces, V.G., and Barco, A. (2019). Immediate and deferred epigenomic signatures of *in vivo* neuronal activation in mouse hippocampus. Nat. Neurosci. *22*, 1718–1730.

Filipkowski, R.K., Rydz, M., Berdel, B., Morys, J., and Kaczmarek, L. (2000). Tactile experience induces c-Fos expression in rat barrel cortex. Learn. Mem. *7*, 116–122.

Filipkowski, R.K., Rydz, M., and Kaczmarek, L. (2001). Expression of c-Fos, Fos B, Jun B, and Zif268 transcription factor proteins in rat barrel cortex following apomorphine-evoked whisking behavior. Neuroscience *106*, 679–688.

Finn, E.H., and Misteli, T. (2019). Molecular basis and biological function of variability in spatial genome organization. Science *365*, 6457.

Finn, E.H., Pegoraro, G., Brandão, H.B., Valton, A.L., Oomen, M.E., Dekker, J., Mirny, L., and Misteli, T. (2019). Extensive heterogeneity and intrinsic variation in spatial genome organization. Cell *176*, 1502–1515.

Hall, M.H., Magalska, A., Malinowska, M., Ruszczycki, B., Czaban, I., Patel, S., Ambrożek-Latecka, M., Zołocińska, E., Broszkiewicz, H., Parobczak, K., et al. (2016). Localization and regulation of PML bodies in the adult mouse brain. Brain Struct. Funct. *221*, 2511–2525.

Hanson, H.H., Reilly, J.E., Lee, R., Janssen, W.G., and Phillips, G.R. (2010). Streamlined embedding of cell monolayers on gridded glass-bottom imaging dishes for correlative light and electron microscopy. Microsc. Microanal. *16*, 747–754.

Hellier, J.L., Patrylo, P.R., Buckmaster, P.S., and Dudek, F.E. (1998). Recurrent spontaneous motor seizures after repeated low-dose systemic treatment with kainate: assessment of a rat model of temporal lobe epilepsy. Epilepsy Res. *31*, 73–84.

Hernández-Fonseca, K., Cárdenas-Rodríguez, N., Pedraza-Chaverri, J., and Massieu, L. (2008). Calcium-dependent production of reactive oxygen species is involved in neuronal damage induced during glycolysis inhibition in cultured hippocampal neurons. J. Neurosci. Res. *86*, 1768–1780.

Ito, S., Magalska, A., Alcaraz-Iborra, M., Lopez-Atalaya, J.P., Rovira, V., Contreras-Moreira, B., Lipinski, M., Olivares, R., Martinez-Hernandez, J., Ruszczycki, B., et al. (2014). Loss of neuronal 3d chromatin organization causes transcriptional and behavioural deficits related to serotonergic dysfunction. Nat. Commun. *5*, 4450.

Jahnke, P., Xu, W., Wülling, M., Albrecht, M., Gabriel, H., Gillessen-Kaesbach, G., and Kaiser, F.J. (2008). The Cohesin loading factor NIPBL recruits histone deacetylases to mediate local chromatin modifications. Nucleic Acids Res. *36*, 6450–6458.

Joo, J.Y., Schaukowitch, K., Farbiak, L., Kilaru, G., and Kim, T.K. (2015). Stimulus-specific combinatorial functionality of neuronal c-fos enhancers. Nat. Neurosci. *19*, 75–83.

Kaczmarek, L., and Chaudhuri, A. (1997). Sensory regulation of immediate-early gene expression in mammalian visual cortex: implications for functional mapping and neural plasticity. Brain Res. Rev. *23*, 237–256.

Kazantsev, A.G., and Thompson, L.M. (2008). Therapeutic application of histone deacetylase inhibitors for central nervous system disorders. Nat. Rev. Drug Discov. *7*, 854–868.

Koressaar, T., and Remm, M. (2007). Enhancements and modifications of primer design program primer3. Bioinformatics *23*, 1289–1291.

Liao, P.S., Chen, T.S., and Chung, P.C. (2001). A fast algorithm for multilevel thresholding. J. Inf. Sci. Eng. *17*, 713–727.

Liao, Y., Smyth, G.K., and Shi, W. (2014). Featurecounts: an efficient general purpose program for assigning sequence reads to genomic features. Bioinformatics *30*, 923–930.

Livak, K.J., and Schmittgen, T.D. (2001). Analysis of relative gene expression data using real-time quantitative PCR and the 2-ΔΔCT method. Methods *25*, 402–408.

Love, M.I., Huber, W., and Anders, S. (2014). Moderated estimation of fold change and dispersion for RNA-seq data with DESeq2. Genome Biol. *15*, 1–21.

Lu, L., Liu, X., Huang, W.K., Giusti-Rodríguez, P., Cui, J., Zhang, S., Xu, W., Wen, Z., Ma, S., Rosen, J.D., et al. (2020). Robust Hi-C maps of enhancer-promoter interactions reveal the function of non-coding genome in neural development and diseases. Mol. Cell *79*, 521–534.e15.

Maag, J.L.V., Panja, D., Sporild, I., Patil, S., Kaczorowski, D.C., Bramham, C.R., Dinger, M.E., and Wibrand, K. (2015). Dynamic expression of long noncoding RNAs and repeat elements in synaptic plasticity. Front. Neurosci. *9*, 1–16.

Maag, J.L.V., Kaczorowski, D.C., Panja, D., Peters, T.J., Bramham, C.R., Wibrand, K., and Dinger, M.E. (2017). Widespread promoter methylation of synaptic plasticity genes in long-term potentiation in the adult brain *in vivo*. BMC Genomics *18*, 250.

Makrantoni, V., and Marston, A.L. (2018). Cohesin and chromosome segregation. Curr. Biol. *28*, 834–840.

Malik, A.N., Vierbuchen, T., Hemberg, M., Rubin, A.A., Ling, E., Couch, C.H., Stroud, H., Spiegel, I., Farh, K.K.H., Harmin, D.A., et al. (2014). Genome-wide identification and characterization of functional neuronal activity-dependent enhancers. Nat. Neurosci. *17*, 1330–1339.

Marco, A., Meharena, H.S., Dileep, V., Raju, R.M., Davila-Velderrain, J., Zhang, A.L., Adaikkan, C., Young, J.Z., Gao, F., Kellis, M., et al. (2020). Mapping the

epigenomic and transcriptomic interplay during memory formation and recall in the hippocampal engram ensemble. Nat. Neurosci. *23*, 1606–1617.

Masiello, I., Siciliani, S., and Biggiogera, M. (2018). Perichromatin region: a moveable feast. Histochem. Cell Biol. *150*, 227–233.

Misteli, T. (2020). The self-organizing genome: principles of genome architecture and function. Cell *183*, 28–45.

Niedojadlo, J., Perret-Vivancos, C., Kalland, K.H., Cmarko, D., Cremer, T., Van Driel, R., and Fakan, S. (2011). Transcribed DNA is preferentially located in the perichromatin region of mammalian cell nuclei. Exp. Cell Res. *317*, 433–444.

Ovesný, M., Křížek, P., Borkovec, J., Švindrych, Z., and Hagen, G.M. (2014). ThunderSTORM: a comprehensive ImageJ plug-in for PALM and STORM data analysis and super-resolution imaging. Bioinformatics *30*, 2389–2390.

O'Sullivan, J.M., Hendy, M.D., Pichugina, T., Wake, G.C., and Langowski, J. (2013). The statistical-mechanics of chromosome conformation capture. Nucl. (United States *4*, 390–398.

Parker, K., Maxson, J., Mooney, A., and Wiley, E.A. (2007). Class I histone deacetylase Thd1p promotes global chromatin condensation in tetrahymena thermophila. Eukaryot. Cell *6*, 1913–1924.

Qiu, Z., and Ghosh, A. (2008). A calcium-dependent switch in a CREST-BRG1 complex regulates activity-dependent gene expression. Neuron *60*, 775–787.

Rajan, W.D., Wojtas, B., Gielniewski, B., Miró-Mur, F., Pedragosa, J., Zawadzka, M., Pilanc, P., Planas, A.M., and Kaminska, B. (2020). Defining molecular identity and fates of CNS-border associated macrophages after ischemic stroke in rodents and humans. Neurobiol. Dis. *137*, 104722.

Rosen, J.B., Fanselow, M.S., Young, S.L., Sitcoske, M., and Maren, S. (1998). Immediate-early gene expression in the amygdala following footshock stress and contextual fear conditioning. Brain Res. *796*, 132–142.

Saha, R.N., Wissink, E.M., Bailey, E.R., Zhao, M., Fargo, D.C., Hwang, J.Y., Daigle, K.R., Fenn, J.D., Adelman, K., and Dudek, S.M. (2011). Rapid activity-induced transcription of Arc and other IEGs relies on poised RNA polymerase II. Nat. Neurosci. *14*, 848–856.

Saha, P.K., and Basu, S.H.E. (2017). Multiscale opening of conjoined fuzzy objects: theory and applications. Physiol. Behav. *176*, 139–148.

Savonenko, A., Filipkowski, R.K., Werka, T., Zielinski, K., and Kaczmarek, L. (1999). Defensive conditioning-related functional heterogeneity among nuclei of the rat amygdala revealed by c-Fos mapping. Neuroscience *94*, 723–733.

Sawyer, I.A., Sturgill, D., and Dundr, M. (2019). Membraneless nuclear organelles and the search for phases within phases. Wiley Interdiscip. Rev. RNA *10*, 1–20.

Schindelin, J., Arganda-Carreras, I., Frise, E., Kaynig, V., Longair, M., Pietzsch, T., Preibisch, S., Rueden, C., Saalfeld, S., Schmid, B., et al. (2012). Fiji: an open-source platform for biological-image analysis. Nat. Methods *9*, 676–682.

Schwarzer, W., Abdennur, N., Goloborodko, A., Pekowska, A., Fudenberg, G., Loe-mie, Y., Fonseca, N.A., Huber, W., Mirny, L., Spitz, F., et al. (2017). Two independent modes of chromatin organization revealed by cohesin removal. Nature *551*, 51–56.

Siddiqui, S.A., Singh, S., Ugale, R., Ranjan, V., Kanojia, R., Saha, S., Tripathy, S., Kumar, S., Mehrotra, S., Modi, D.R., et al. (2019). Regulation of HDAC1 and HDAC2 during consolidation and extinction of fear memory. Brain Res. Bull. *150*, 86–101.

Skupien-Jaroszek, A., Walczak, A., Czaban, I., Pels, K.K., Szczepankiewicz, A.A., Krawczyk, K., Ruszczycki, B., Wilczynski, G.M., Dzwonek, J., and Magalska, A. (2021). The interplay of seizures-induced axonal sprouting and transcription-dependent Bdnf repositioning in the model of temporal lobe epilepsy. PLoS One *16*, 1–18.

Sliwińska, M.A., Cały, A., Borczyk, M., Ziółkowska, M., Skonieczna, E., Chilimoniuk, M., Bernaś, T., Giese, K.P., and Radwanska, K. (2020). Long-Term memory upscales volume of postsynaptic densities in the process that requires autophosphorylation of αCaMKII. Cereb. Cortex *30*, 2573–2585.

Spagnol, S.T., and Dahl, K.N. (2016). Spatially resolved quantification of chromatin condensation through differential local rheology in cell nuclei fluorescence lifetime imaging. PLoS One *11*, 1–19.

Strom, A.R., Emelyanov, A.V., Mir, M., Fyodorov, D.V., Darzacq, X., and Karpen, G.H. (2017). Phase separation drives heterochromatin domain formation. Nature *547*, 241–245.

Szepesi, Z., Bijata, M., Ruszczycki, B., Kaczmarek, L., and Wlodarczyk, J. (2013). Matrix metalloproteinases regulate the formation of dendritic spine head protrusions during chemically induced Long-Term Potentiation. PLoS One *8*, e63314.

Tao-Cheng, J.H. (2018). Stimulation-induced structural changes at the nucleus, endoplasmic reticulum and mitochondria of hippocampal neurons. Mol. Brain *11*, 1–14.

Thanh, D.C., Ngoc, C.T.B., Nguyen, N.L., Vu, C.D., Van Tung, N., and Nguyen, H.H. (2020). De novo NIPBL mutations in vietnamese patients with cornelia de lange syndrome. Med. *56*, 5–7.

Trzaskoma, P., Ruszczycki, B., Lee, B., Pels, K.K., Krawczyk, K., Bokota, G., Szczepankiewicz, A.A., Aaron, J., Walczak, A., Śliwińska, M.A., et al. (2020). Ultrastructural visualization of 3D chromatin folding using volume electron microscopy and DNA *in situ* hybridization. Nat. Commun. *11*, 1–9.

Untergasser, A., Cutcutache, I., Koressaar, T., Ye, J., Faircloth, B.C., Remm, M., and Rozen, S.G. (2012). Primer3-new capabilities and interfaces. Nucleic Acids Res. *40*, 1–12.

Vaňková Hausnerová, V., and Lanctôt, C. (2017). Chromatin decondensation is accompanied by a transient increase in transcriptional output. Biol. Cell *109*, 65–79.

Vernole, P., Neri, G., and Serra, A. (1984). A new banding technique of rat Rattus norvegicus chromosomes. Hereditas *101*, 199–204.

Vian, L., Pękowska, A., Rao, S.S.P., Kieffer-Kwon, K.R., Jung, S., Baranello, L., Huang, S.C., El Khattabi, L., Dose, M., Pruett, N., et al. (2018). The energetics and physiological impact of cohesin extrusion. Cell *173*, 1165–1178.e20.

Volmar, C.H., and Wahlestedt, C. (2015). Histone deacetylases (HDACs) and brain function. Neuroepigenetics *1*, 20–27.

Walczak, A., Szczepankiewicz, A.A., Ruszczycki, B., Magalska, A., Zamlynska, K., Dzwonek, J., Wilczek, E., Zybura-Broda, K., Rylski, M., Malinowska, M., et al. (2013). Novel higher-order epigenetic regulation of the Bdnf gene upon seizures. J. Neurosci. *33*, 2507–2511.

Wilczynski, G.M., Konopacki, F.A., Wilczek, E., Lasiecka, Z., Gorlewicz, A., Michaluk, P., Wawrzyniak, M., Malinowska, M., Okulski, P., Kolodziej, L.R., et al. (2008). Important role of matrix metalloproteinase 9 in epileptogenesis. J. Cell Biol. *180*, 1021–1035.

Yamada, T., Fischle, W., Sugiyama, T., Allis, C.D., and Grewal, S.I.S. (2005). The nucleation and maintenance of heterochromatin by a histone deacetylase in fission yeast. Mol. Cell *20*, 173–185.

Yap, E.L., and Greenberg, M.E. (2018). Activity-regulated transcription: bridging the gap between neural activity and behavior. Neuron *100*, 330–348.

Yu, X., Zhan, X., D'Costa, J., Tanavde, V.M., Ye, Z., Peng, T., Malehorn, M.T., Yang, X., Civin, C.I., and Cheng, L. (2003). Lentiviral vectors with two independent internal promoters transfer high-level expression of multiple transgenes to human hematopoietic stem-progenitor cells. Mol. Ther. *7*, 827–838.

Yu, G., Wang, L.G., Han, Y., and He, Q.Y. (2012). ClusterProfiler: an R package for comparing biological themes among gene clusters. Omi. A. J. Integr. Biol. *16*, 284–287.

CellPress
OPEN ACCESS

STAR★METHODS

KEY RESOURCES TABLE

REAGENT or RESOURCE	SOURCE	IDENTIFIER
Antibodies		
Anti-NeuN chicken polyclonal IgY	Millipore	Cat# ABN91;RRID:AB_11205760
Anti-c-FOS guinea pig polyclonal antiserum	Synaptic Systems	Cat# 226 004; RRID:AB_2619946
Anti-CamKII mouse monoclonal IgG_1	Santa Cruz Biotechnology	Cat# Sc-32288;RRID:AB_626787
Anti-macroH2A mouse monoclonal IgG2a	Santa Cruz Biotechnology	Cat# Sc-377452; RRID:AB_2904601
Anti-H4K20me2/3 mouse monoclonal IgG1 [6F8-D9]	Abcam	Cat# Ab78517;RRID:AB_1951279
Anti-H3K9ac mouse monoclonal IgG1 [AH3-120]	Abcam	Cat# Ab12179; RRID:AB_298910
Anti-H3K4me3 rabbit polyclonal antiserum	Active Motif	;Cat# 39159RRID:AB_2615077
Anti-H3K9me2 mouse monoclonal IgG2a [mAbcam 1220]	Abcam	Cat# Ab1220; RRID:AB_449854
Anti-H3K9me2/3 rabbit polyclonal IgG [C36B11]	Cell Signalling Technology	Cat# 9733S; RRID:AB_2616029
Anti-H3K27me3 rabbit polyclonal IgG	Millipore	Cat# 07-449; RRID:AB_310624
Anti-H3K56ac rabbit polyclonal IgG	Abcam	Cat# Ab71956; RRID:AB_10861799
Anti-H2Bac rabbit polyclonal antiserum	Kindy provided by A. Barco	
Anti-HDAC1 rabbit polyclonal IgG	Abcam	Cat# Ab19845; RRID:AB_470299
Anti-HP1α rabbit polyclonal IgG	Cell Signaling Technology	Cat# 2616S; RRID:AB_2070987
Anti-HP1β rabbit polyclonal IgG	Cell Signaling Technology	Cat# 8676S; RRID:AB_11217816
Anti-Nucleolin rabbit polyclonal IgG	Abcam	Cat# Ab22758; RRID:AB_776878
Anti-polIIS2P rabbit polyclonal IgG	Abcam	Cat# Ab5095; RRID:AB_304749
Anti-SF3A66 mouse monoclonal IgG1 [4G8]	Abcam	Cat# Ab77800; RRID:AB_2186364
anti-digoxygenin antibody conjugated with Rhodamine (Roche)	Roche	Cat# 11207750910; RRID:AB_514501
Goat Anti-Mouse IgG H&L (HRP) preadsorbed	Abcam	Cat# Ab97040; RRID:AB_10698223
Alexa Fluor® 488 AffiniPure $F(ab')_2$ Fragment Donkey Anti-Mouse IgG (H + L)	Jackson ImmunoResearch Labs	Cat# 715-546-151; RRID:AB_2340850
Alexa Fluor® 488 AffiniPure $F(ab')_2$ Fragment Donkey Anti-Rabbit IgG (H + L)	Jackson ImmunoResearch Labs	Cat# 711-546-152; RRID:AB_2340619
$Cy^{TM}3$ AffiniPure $F(ab')_2$ Fragment Donkey Anti-Rabbit IgG (H + L)	Jackson ImmunoResearch Labs	Cat# 711-166-152; RRID:AB_2313568
Alexa Fluor® 647 AffiniPure $F(ab')_2$ Fragment Donkey Anti-Chicken IgY (IgG) (H + L)	Jackson ImmunoResearch Labs	Cat# 703-606-155; RRID:AB_2340380
Goat anti-Guinea Pig IgG (H + L) Alexa Fluor 647	ThermoFisher Scienfic	Cat# A21450; RRID:AB_2735091
Goat Anti-Mouse IgG H&L (HRP)	Abcam	Cat# Ab97040; RRID:AB_10698223
Donkey Anti-Rabbit IgG H&L (HRP)	Abcam	Cat# Ab205722; RRID:AB_2904602
Bacterial and virus strains		
XL1-Blue High Cloning Efficiency	Agilent	200236
DH5alpha subcloning efficiency	New England Biolabs	C2988J
2^{ND} generation lentiviral vectors		
Chemicals, peptides, and recombinant proteins		
α-Amanitine	Millipore	Cat# A2263
Anacardic Acid	APExBIO	Cat# A4488

(*Continued on next page*)

Continued

REAGENT or RESOURCE	SOURCE	IDENTIFIER
A 196	Cayman Chemical Company	Cat# 18317
BIX 01294	APExBIO	Cat# A1909
CI 994	Cayman Chemical Company	Cat# EPI009
DRB	Abcam	Cat# ab120939
JQ 1	APExBIO	Cat# A1910
MI 192	Cayman Chemical Company	Cat# 18288
Romidepsin	Cayman Chemical Company	Cat# 17130
Trichostatin A (TSA)	Millipore	Cat# EPI009
FK506	Enzo	Cat# ALX380008M001
Oligomycin	Millipore	Cat# O4876
sodium iodoacetate	Millipore	Cat# 19148
1,6-hexanodiol	Millipore	Cat# 240117
Forskolin	Millipore	Cat# F6886
Rolipram	Millipore	Cat# R6520
Picrotoxin	Millipore	Cat# P1675
DL-2-amino-5-phosphopentanoic acid	Millipore	Cat# A5282
Tetrodotoxin (TTX)	Millipore	ab120054
Laminin	Roche	Cat# 11243217001
Paraformaldehyde	Millipore	Cat# P6148
Heat Inactivated Fetal Bovine Serum FBS	Life Technologies	Cat# 16140071
Poli-D-lysine	Millipore	Cat# P7886
OptiMEM	Gibco	Cat# 11058021
Neurobasal A 1x	Life Technologies	Cat# 10888022
MEM 1x	Life Technologies	Cat# 51200046
B-27	Life Technologies	Cat#17504044
Papain	Cell Systems Biotechnologie Vertrieb GmbH	Cat#LS003126
MEM Non-essential Amino Acid Solution (100×)	Millipore	Cat#M7145
DMSO	Millipore	Cat# 276855
Critical commercial assays		
Click-iT RNA Alexa Fluor 488 Imaging Kit	Invitrogen	C-10425
NEBuilder HiFi DNA Assembly Master Mix	NEB	E2621L
KAPA Stranded mRNA Sample Preparation Kit	Kapa Biosystems	KK8420
Deposited data		
RNA-seq data	This paper	GEO: GSE166599
Western Blot original data	This paper	Mendeley: https://doi.org/10.17632/ghp9xtn3tw.1
Experimental models: Organisms/strains		
Wistar rats, weight 170–250 g, 2–3 months old males	Mossakowski Medical Research Centre.	N/A
C57BL6 mice, weight 20-30 g 2–3 months old males	Mossakowski Medical Research Centre.	N/A
Wistar rat's P0 pups	Nencki Institute Animal House	N/A
Oligonucleotides		
EF.CMV.RFP Forward: GGATGCGGTGGGCTCTA TGGGGAATTAGCTTGGTACTAATACG	This study	N/A

(*Continued on next page*)

Continued

REAGENT or RESOURCE	SOURCE	IDENTIFIER
EF.CMV.RFP Reverse: GCACTCATACGCAGGACAT GAATTCCCACTCCTTTCAAGA	This study	N/A
HDAC1 Flag Forward: AGCTGCTCGAGCTCAAGCTT GGATCCGAATTCACGATGGC	This study	N/A
HDAC1 Flag Reverse: ATTAGTACCAAGCTAATTCCCCAT AGAGCCCACCGCATCC	This study	N/A
pSynapsin_eGFP Forward: TCTTGAAAGGAGTGGGAATTCATG TCCTGCGTATGAGTGC	This study	N/A
pSynapsin_eGFP Reverse: GCCATCGTGAATTCGGATCCAAG CTTGAGCTCGAGCAGCT	This study	N/A
HDAC1 forward: GCGAGCAAGATGGCGCAGACT	This study	N/A
HDAC1 reverse: GTGAGGCTTCATTGGGTGCCCT	This study	N/A
GAPDH forward: AGTTCAACGGCACAGTCAAG	This study	N/A
GAPDH reverse: TACTCAGCACCAGCATCACC	This study	N/A
18S rRNA forward: CCCAGTAAGTGCGGGTCATA	This study	N/A
18S rRNA reverse: GGCCTCACTAAACCATCCAA	This study	N/A
Recombinant DNA		
pGFP-C-shLenti_scrambled	Origene	TL702923
pGFP-C-shLenti_shHDAC1	Origene	TL702923
EF.CMV.RFP	Addgene, (Emiliani et al., 1998)	RRID:Addgene_17619
HDAC1-FLAg	Addgene, (Yu et al., 2003)	RRID:Addgene_13820
pSynHDAC1FlagRFP	This study	N/A
pSynapsin_eGFP	kindly provided by Piotr Michaluk	N/A
Software and algorithms		
Video Fear Conditioning "Video Freeze®" Software	Med Associates Inc.	SOF-843
SymPhoTime 64 Fluorescence Lifetime Imaging and Correlation Software	PicoQuant	N/A
Fiji	(Schindelin et al., 2012)	N/A
ThunderSTORM ImageJ plug-in	(Ovesný et al., 2014)	N/A
PartSeg Software	(Bokota et al., 2021)	N/A
Multiscale Opening algorithm	(Saha et al., 2017)	N/A
STAR program	(Dobin et al., 2013)	N/A
Counts algorithm	(Liao et al., 2014)	N/A
DESeq2	(Love et al., 2014)	N/A
ClusterProfiler package	(Yu et al., 2012)	N/A
Primer3 software	(Koressaar and Remm, 2007; Untergasser et al., 2012)	N/A
Image Studio Lite software	(Licor)	N/A
Prism 5.0	GraphPad	N/A

RESOURCE AVAILABILITY

Lead contact

Further information and requests for resources and reagents should be directed to and will be fulfilled by the lead contact, Adriana Magalska (a.magalska@nencki.edu.pl).

Materials availability

Plasmids generated in this study will be shared by the lead contact upon request.

Data and code availability

- RNA-seq data have been deposited at GEO and are publicly available as of the date of publication. Accession numbers are listed in the key resources table. Original western blot images have been deposited at Mendeley Data and are publicly available as of the date of publication. The DOI is listed in the key resources table. Microscopy data reported in this paper will be shared by the lead contact upon request.
- This paper does not report original code.
- Any additional information required to reanalyze the data reported in this paper is available from the lead contact upon request.

EXPERIMENTAL MODEL AND SUBJECT DETAILS

Animals

Cell cultures were acquired from P0 Wistar rat's pups obtained from the Nencki Institute Animal House. The animal experiments were performed on young, adult male Wistar rats, weight 170–250 g, and on 2–3 months old male C57BL6 mice, weight 20–30 g, obtained from Mossakowski Medical Research Institute. The animals were kept under natural 12 h light/dark cycle in Plexiglass cages, in a room thermostatically maintained at 22 ± 1°C, with unlimited food and water supplies.

METHOD DETAILS

Induction of seizures

Seizures in rats were evoked by three doses of kainate (5 mg/kg, Sigma Aldrich) in 0.9% solution of saline, pH 7, administered intraperitoneally in 1 h intervals to limit the mortality rate, and scored as described by Hellier et al. (Hellier et al., 1998). The animals were taken for further studies regardless of whether they fulfilled the criterion of the full status epilepticus or not, and were sacrificed 2h after the first signs of seizures.

Fear conditioning

Animals

The rats were kept in groups of two per cage for 7 days. Twelve male Wistar rats, 8 weeks old at the time of conditioning, were divided into 2 conditions: naive (n = 6) and shocked (n = 6).

Apparatus

Training and testing took place in the automated observation chamber, *i.e.* conditioning box (30.0 × 24.0 × 21.0 cm) of Near Infrared Video Fear Conditioning System (Med Associates Inc.), constructed from aluminum (side walls) and Plexiglas (rear wall, ceiling, and front door) with stainless-steel grid floor wired to Aversive Stimulator (ENV-414S, Med Associates Inc.) and installed inside Sound-Attenuating Cubicle (Med Associates Inc.) located in an isolated room. The lights within the box were switched off and ventilation fan supplied background noise. Chambers were cleaned with a 1% acetic acid solution between animals. The freezing behavior was recorded by Fire Wire Video Camera (Med Associates Inc.), measured and analyzed using Video Freeze Software (Med Associates Inc.).

Procedure

The naive rats served as controls and were not placed in the chamber. Rats from the shocked group were placed in the testing chamber for 2 min, then given 2-s-long, 1.5 mA foot-shock, left in the chamber for additional 4 min and kept for 2 h single caged. After that, they were returned to the chamber and tested for 3 min and then immediately sacrificed. Similar fear conditioning procedure was used before to investigate immediate-early gene expression in rats (Rosen et al., 1998). The rats from the shocked group expressed a minimal level of freezing (1.1 ± 1.1%) during the first 2 min of chamber exploration. The freezing during 4 min immediately following the foot-shock increased to 28.8 ± 10.3% ($P < 0.05$) and remained increased 2 h later (32.0 ± 8.3%, $P < 0.05$; both Wilcoxon test), which confirms that short-term memory was formed.

Procedures were performed with the consent of the first Local Ethical Committee in Warsaw (Permission numbers LKE 306/2017, LKE 774/2015 and LKE 295/217).

All animals were euthanized with an overdose of pentobarbital sodium (Nembutal 150 mg/kg, i.p.) and perfused with 4% paraformaldehyde in PBS at the end of the experiments, and the brain tissues were collected.

In vivo LTP by High Frequency Stimulation

High Frequency Stimulation (HFS) was applied as described in Maag et al. (Maag et al., 2015, 2017). In anesthetized adult, male Sprague-Dawley rats, electrodes were positioned for the selective unilateral stimulation of the medial perforant path fibers in the angular bundle. Recordings of the evoked field potentials were obtained with borosilicate glass micropipettes (tip diameter 1–5 μm), filled with 1 mM NaCl in the hilar region of the dentate gyrus. During the whole experiment, test pulses were applied at 0.033 Hz, except for the HFS period. After stabilization of responses, the base-line recording was performed for a subsequent 45 min, which was followed by HFS induced in three sessions with 5 min pause between each session. Each HFS session consisted of four 400 Hz stimulus trains (8 pulses/burst) with a 10s interval with a total HFS duration of 10.5 min and a total pulse number of 128. This research was approved by Norwegian National Research Ethics Committee in compliance with EU Directive 2010/63/EU, ARRIVE guidelines. Persons involved in animal experiments have Federation of Laboratory and Animal Science Associations (FELASA) C course certificates and training. The rats used to obtain brain tissue were anesthetized using urethane and sacrificed without suffering.

Cell culture

Primary hippocampal neurons from Wistar rat pups at P0 were cultured in 6-well plates (VWR) or in 24-well plates (VWR) on 12 mm glass coverslips (VWR) coated with poly-D-lysine (Sigma Aldrich) and laminin (Roche). After tissue homogenization, cells were counted in a Bürker chamber and seeded at the density of ∼300,000 cells or ∼75,000 cells per well, respectively. After 1.5–2 h, plating medium (MEM supplemented with 10% fetal bovine serum, 0.45% glucose, 2 mM glutamine and penicillin/streptomycin 100 U/ml–100 μg/mL) was replaced with defined maintenance medium (neurobasal supplemented with B27, 2 mM glutamine and penicillin/streptomycin 100 U/ml–100 μg/mL).

Chemical LTP

Chemically-induced long-term potentiation of synaptic transmission (cLTP) was induced according to previously published protocol (Szepesi et al., 2013) by adding 50 μM forskolin (Sigma Aldrich), 50 nM rolipram (Sigma Aldrich), and 200 μM picrotoxin (Sigma Aldrich) to the medium on DIV13-15. These compounds directly stimulate the biochemical machinery underlying synaptic plasticity by increasing cAMP levels (Szepesi et al., 2013). As the chemicals were dissolved in DMSO, the same amount of the solvent was added to the medium of the control. Cells were incubated with the solutions for 1 h (for cells with silenced HDAC1) or 2 h and then immediately fixed. Fixation step was performed using 4% PFA freshly prepared from 16% stock (Thermo Scientific, dissolved 1:4 in 1xPBS) for 10 min RT. Next, PFA was exchanged for 1xPBS and the slides were kept at 4°C until further use. To prevent bacteria growth, sodium azide was added to 0.002% concentration.

Stimulation with potassium chloride

Stimulation with potassium chloride was performed according to Malik et al. (Malik et al., 2014). Prior to KCl depolarization, neurons were silenced with 1 μM tetrodotoxin (TTX; Abcam), and 100 μM DL-2-amino-5-phosphopentanoic acid (DL-AP5; Sigma Aldrich) for 16 h. The next day, the neurons were stimulated by adding warmed KCl depolarization buffer (170 mM KCl, 2 mM $CaCl_2$, 1 mM $MgCl_2$ and 10 mM 4-(2-hydroxyethyl)-1-piperazineethanesulfonic acid (HEPES)) directly to the neuronal culture to a final concentration of 55 mM KCl in the neuronal culture medium.

RNA labeling/EU incorporation assay

Cells were treated with 200 mM DRB or DMSO, as a control, for 2 h, and then stimulated for 2 h using cLTP mixture. For the last 30 min of stimulation 1mM 5-ethynyl uridine (EU) was added. Next, cells were washed with warm 1xPBS and fixed with 4% PFA for 15 min in RT. EU was detected using Click-iT RNA Alexa Fluor 488 Imaging Kit (Invitrogen) according to manufacturer's instructions. Briefly, cells were washed with 1xPBS and permeabilized with 0.5% Triton X-100 for 15 min. The cells were incubated in Click-iT reaction cocktail (Component C, CuSO4, Alexa 488 and Buffer Additive) for 30 min in RT in darkness. Afterward, cells were washed with Click-iT Reaction Rise Buffer and 1xPBS. Chromatin was visualized with Hoechst 33,342 (Thermo Scientific). Slides were mounted with Vectashield (Vector Lab) and imaged on the same day.

Propidium iodide exclusion test

Cells were stimulated for 2 h with cLTP inducing mixture, DMSO as a negative control or 100 μM kainate as a positive control. Viability test was performed by adding propidium iodide to the medium to 1μg/mL concentration for 2 min. Next, the cells were fixed in 4% PFA, mounted with Vectashield (Vector Lab) and imaged immediately. Living cells with intact cell membranes exclude PI, while dead cells accumulate dye in the nucleus, where PI strongly binds to the DNA.

Washing out of the cLTP inducing mixture

Hippocampal neurons were stimulated for 2 h to induce cLTP or incubated for the same time with a vehicle (DMSO). After 2 h of stimulation, the cells were washed with a fresh batch of conditioned culture medium. Samples were fixed at 0, 3, 6 and 24 h' time points and DNA was visualized with Hoechst 33,432 using confocal microscopy.

HDAC1 silencing and Addback experiments

Silencing plasmids pGFP-C-shLenti_scrambled and pGFP-C-shLenti-HDAC1 (Origene TR30023) were delivered to cultured neurons, growing in 24-well plates, at DIV3, using lentiviral vector. Next day, the medium with the virus was changed for the pre-conditioned medium and neurons were left to grow till DIV13-15. For add back experiments, a day after transduction, neurons (DIV4) were transfected with pSynHDAC1FlagRFP plasmid (500 μg/well) using Lipofectamine3000 (Thermo Scientific) according to manufacturer instructions. Cells were incubated with Lipofectamine/DNA complexes in transfecting medium (OptiMEM, 2% B-27 Supplement, 1 mM pyruvate, 0.5 mM GlutaMAX, 25 μM β-mercaptoethanol) for 45 min 37°C, 5% CO_2 in humidified incubator. Afterward, the medium was replaced with their conditioned maintenance medium.

Lentiviruses used in silencing experiments were produced in the Laboratory Of Animal Models, core facility of Nencki Institute of Experimental Biology.

Treatments

All treatments were performed on cultured neurons DIV13-15. Inhibitor concentrations and incubation times are indicated in the table below. For each inhibitor, incubation step was followed by 2 h of cLTP activation with the exception of hexanediol, which was added for the last 5 min of cLTP activation. At the end, cells were washed once with 1xPBS and fixed with 4% PFA.

Reagent	Role	Concentrations tested	Treatment times
α-Amanitine	potent inhibitor of eukaryotic RNA pol II and a mild inhibitor of RNA pol III; binds with high affinity to the largest subunit of RNAPII, RPB1	32μg/μL; 10 μg/μL	3 h and 12 h
Anacardic Acid	inhibitor of the histone acetyltransferase p300/CBP	1 μM	24 h
A 196	an inhibitor of SUV420H1 and SUV420H2 methyltransferases	1–500 μM	2 h
BIX 01294	a G9a methyltransferase inhibitor	1–2 μM	2 h, 6 h, 12 h, 24 h
CI 994	an inhibitor of HDAC1, 2, 3, and 8	10–100 μM	2 h
DRB	selective inhibitor of Cdk9 (IC50 = 3 μM), the kinase of the positive transcription elongation factor b (P-TEF-b) required for processive transcription elongation by RNA polymerase II	200 μM	1 h and 3 h
JQ 1	a competitive inhibitor of bromodomain binding to acetylated histones	1 μM	24 h
MI 192	an inhibitor specifically targeting HDAC2 and HDAC3	1–10 μM	2 h
Romidepsin	an inhibitor of HDAC1 and HDAC2	250 nM	2 h
Trichostatin A (TSA)	pan-inhibitor of histone deacetylases	25–250 nM	2 h
FK506	blocks the activation of calcineurin	10 μM	2 h
Oligomycine	an inhibitor of ATP synthase	5–50 μg/mL	5 min
sodium iodoacetate	an inhibitor of glycolysis, which irreversibly inhibits the glycolytic enzyme glyceraldehyde-3-phosphate dehydrogenase (GAPDH)	1 mM	5 min
1,6-hexanediol	An aliphatic alcohol shown to specifically break weak hydrophobic bonds engaged in LLPS	5%	5 min

Table: inhibitors, concentrations and incubation times used in experiments

Cloning

pSynHDAC1FLAgRFP plasmid was constructed using NEBuilder HiFi DNA Assembly Master Mix (NEB) using EF.CMV.RFP (Addgene #17619), HDAC1-FLAg (Addgene #13820) and pSynapsin_eGFP (kindly provided by Piotr Michaluk) according to manufacturer's instructions. Fragments were amplified with following primers:

EF.CMV.RFP F: – GGATGCGGTGGGCTCTATGGGGAATTAGCTTGGTACTAATACG.

EF.CMV.RFP R: – GCACTCATACGCAGGACATGAATTCCCACTCCTTTCAAGA.

HDAC1 Flag F: – AGCTGCTCGAGCTCAAGCTTGGATCCGAATTCACGATGGC.
HDAC1 Flag R: – ATTAGTACCAAGCTAATTCCCCATAGAGCCCACCGCATCC.
pSynapsin_eGFP F: – TCTTGAAAGGAGTGGGAATTCATGTCCTGCGTATGAGTGC.
pSynapsin_eGFP R: – GCCATCGTGAATTCGGATCCAAGCTTGAGCTCGAGCAGCT.
using Phusione Hot Start II Hight Fidelity Polymerase (Thermo Scientific).

Western blotting

Proteins were extracted from DIV13-15 neurons using RIPA buffer (Merck-Millipore) supplemented with 1x cOmplete Protease Inhibitor cocktail (Roche), 1 μM NaF (Sigma Aldrich) and 1 mM PMSF (Sigma Aldrich) according to manufacturer's instructions. Cells were washed with 1xPBS and incubated with lysis buffer for 30 min on ice. Afterward, the cells were scraped and transferred to sterile Eppendorf tubes. Complete cell disruption was ensured by repeated forcing the lysates through the syringe needle (0.5 mm in diameter). Next, lysates were centrifuged (16,000 ×g, for 20 min at 4°C) and protein concentration in supernatants was determined using a Bradford protein assay (Bio-Rad). Finally, supernatants were mixed with Laemmli buffer, heated for 5 min at 95°C and stored in −20°C. Proteins (15 μg of each sample with exception for macroH2A blots for which 30 μg was used) were separated on polyacrylamide gels (12–15% depending on the molecular mass of the protein) in denaturating conditions (0.1% SDS) and electroblotted onto Immobilon-P Transfer Membrane (Merck-Millipore) 20 V for 1 h at RT. Then, the blots were blocked in 5% non-fat milk dissolved in 1xTBST (1xTBS with 0.01% Tween 20 (Sigma Aldrich)) for 1 h at RT. Immunodetection was carried at 4°C overnight using primary antibody diluted in 1% milk in 1xTBST (list of antibodies used is provided in the Table below). Afterward, the membranes were washed with 1xTBST and incubated with anti-Rabbit (1:5000, ab205722, Abcam) or anti-Mouse (1:5000, ab97040, Abcam) horseradish peroxidase-conjugated secondary antibody for 1 h at RT. Protein bands were visualized using Immobilon Forte Western HRP substrate (Merck-Millipore). To visualise total protein levels the membranes were washed with TBS, stained with Ponceau Red for 30 min in RT, washed again with ddH_2O and left to air-dry for 1 h. All images were obtained using a G-Box gel documentation system (Syngene). Densitometric analyses of specific protein bands were carried using Image Studio Lite software (Licor). Specific protein bands were normalised to total protein signal in a specific line.

Immunodetection

Immunofluorescence staining was performed according to routine procedures (Hall et al., 2016). Fixed DIV13-15 neurons were washed in 1xPBS and permeabilized with 0.35% Triton X-100 (Sigma Aldrich) for 3 min at RT. Incubation with primary antibodies (list and dilutions in table below) diluted in 1% BSA in PBS with 0.1% Triton X-100 (PBST) was carried either for 1 h, at RT or overnight in 4°C in a humid chamber. Signals were detected with secondary antibodies conjugated with fluorophores diluted 1:500 in 1% BSA in PBST. Samples were counterstained with Hoechst 33,342 for 10 min RT, washed 3x for 5 min with PBST and mounted using Vectashield (Vector Laboratories) and analyzed using a confocal microscope.

Antigen	Dilution used	Incubation time
NeuN	1:1000 (IF)	1 h RT or 16 h, 4°C (IF)
cFos	1:1000 (IF)	1 h RT or 16 h, 4°C (IF)
CamKII	1:200 (IF)	1 h RT or 16 h, 4°C (IF), 16 h, 4°C (WB)
GAD67	1: 100 (IF)	16 h 4°C (IF)
macroH2A	1:100 (IF) 1:500 (WB)	1 h RT or 16 h, 4°C (IF) 16 h, 4°C (WB)
H4K20me2/3	1:500 (IF) 1:1000 (WB)	16 h 4°C (IF, WB)
H3K9ac	1:1000 (IF, WB)	1 h RT or 16 h 4°C (IF); 16 h 4°C (WB)
H3K4me3	1:200 (IF) 1:1000 (WB)	1 h RT or 16 h 4°C (IF); 16 h 4°C (WB)
H3K9me2	1:500 (IF) 1:500 (WB)	1 h RT or 16 h 4°C (IF); 16 h 4°C (WB)
H3K9me2/3	1:100 (IF) 1:1000 (WB)	16 h 4°C (IF, WB)
H3K27me3	1:200 (IF) 1:1000 (WB)	16 h 4°C (WB)
H3K56ac	1:1000 (IF, WB)	16 h 4°C (WB)
H2Bac	1: 1000 (IF)	16 h 4°C (IF)
HDAC1	1:1000 (IF, WB)	1 h RT or 16 h 4°C (IF); 16 h, 4°C (WB)
HP1α	1:1000 (WB)	16 h, 4°C (WB)
HP1β	1:800 (IF) 1:1000 (WB)	16 h, 4°C (IF, WB)
Nucelolin	1:1000 (IF)	16 h, 4°C (IF, WB)
polIIS5P	1:1000 (IF) 1:100 (WB)	16 h, 4°C (IF, WB)
SF3A66	1:400 (IF) 1:500 (WB)	16 h, 4°C (IF, WB)

Table: antibodies, concentrations and incubation times used in experiments

Immunodetection on brain slices

Animals were injected intraperitoneally with a lethal dose of sodium pentobarbital (130 mg/kg) and perfused with 4% PFA in ice-cold PBS. Collected brains were postfixed at 4°C, overnight in 4% PFA in PBS, soaked in 30% sucrose, flash freezed, cryosectioned to 40 μm slices and stored for further use in −20°C in the antifreezing medium (30% glycerol, 30% ethylene glycol, 10 mM phosphate buffer pH 7.4). Immunostaining for c-FOS and neuronal markers was performed using our standard staining protocol (Wilczynski et al., 2008).

3D DNA-FISH

DNA-FISH was performed according to Cremer et al. (Cremer et al., 2012) with minor modifications. Probes against chromosome 1 (biotin-labeled) and 16 (digoxygenin-labeled) were purchased from (ChromBios). Cells, fixed with 4% PFA, were permeabilized with 0.5% Triton X-100 in 1xPBS solution for 20 min at RT, followed by the incubation in 0.1 N hydrochloric acid for 10 min at RT. Next, cells were washed in 2xSSC for 5 min and incubated for 30 min in 2xSSC with 50% formamid solution in RT. Probes were dissolved 1:10 in hybridization buffer (ChromBios) and applied on slides. Denaturation step was carried for 7 min at 85°C, followed by overnight incubation in humid chamber at 37°C. The unspecifically bound probe was removed by a series of high-stringency washes with 2xSSC with 50% formamid at 37°C, 0.1xSSC at 60°C and 4xSSC with 0.2% Triton X-100 at RT. Probes were detected using either avidin conjugated with Alexa 488 (Invitrogen) or anti-digoxygenin antibody conjugated with Rhodamine (Roche), diluted 1:1000 in PBST for 1 h at RT. Finally, chromatin was visualized with Hoechst 33,342 during 10 min incubation in RT. Slides were mounted using Vectashield (Vector Laboratories).

EM sample preparation

Cells growing on a 12 mm glass coverslips were fixed with 2% PFA (Sigma Aldrich), and 1% glutaraldehyde (EMS, EM grade) in 0.2 M HEPES pH 7.3 and prepared for electron microscopy according to the published protocol (Deerinck et al., 2010), with minor changes (Sliwińska et al., 2020). Briefly, cells were post-fixed with 1% aqueous solution of osmium tetroxide (Agar Scientific) and 1.5% potassium ferrocyanide (Sigma Aldrich) in phosphate buffer for 30 min on ice. Then, samples were immersed in 1% aqueous thiocarbohydrazide (Sigma Aldrich) for 20 min, post-fixed with 2% aqueous solution of osmium tetroxide (Sigma Aldrich) for 20 min (all at room temperature) and incubated in 1% aqueous uranyl acetate (Serva) at 4°C overnight. The next day, samples were exposed to 0.66% lead aspartate for 30 min at 60°C, dehydrated with increasing dilutions of ethanol, infiltrated with Durcupan resin (Sigma Aldrich), embedded using BEEM capsules according to the published protocol (Hanson et al., 2010). The resin blocks were trimmed and cut with an ultramicrotome (ultracut R, Leica) and ultrathin sections (65 nm thick) were collected on formvar-coated copper grids, mesh 100 (Agar Scientific).

Transmission electron microscopy

Specimen grids were examined with a transmission electron microscope JEM 1400 (JEOL Co.), equipped with a 11 megapixel TEM camera MORADA G2 (EMSIS GmbH|).

TEM experiments were done in the Laboratory of Electron Microscopy, core facility of Nencki Institute of Experimental Biology.

Confocal microscopy

Fluorescence images were captured using Zeiss LSM800 Airyscan or LSM780 Microscope (Zeiss) equipped with 63× PlanApo oil immersion objective (NA 1.4). Pixel size was set to 70 nm in xy-direction and 190 nm in z-direction, according to the Nyquist criterion. Confocal pinhole was set to 1 Airy unit for each channel. Fluorescence was excited with the following lasers: 405nm diode, 488nm argon ion (LSM 780) or diode (LSM800) 561nm DPSS, 640 nm diode (LSM800) or 633 nm HeNe (LSM780). Cross-talk between the fluorophores was eliminated by adjustment of the spectral ranges of the PMT detectors and sequential scanning of the images.

Fluorescence lifetime imaging

FLIM experiments were conducted according to Spagnol and Dahl (Spagnol and Dahl, 2016). Fixed cells were stained with Hoechst 33,342 dye (Invitrogen) for 30 min RT and mounted using Vectashield Mountig Medium (Vector Laboratories). Images were collected using SP8 confocal microscope (Leica), 63× PlanApo oil immersion objective (NA 1.4) and confocal pinhole set to 2 Airy units. Hoechst fluorescence was excited with a 405 nm pulsed diode laser at 40 mHz. The fluorescence was detected in 425–470 nm range with an SPAD detector. The fluorescence lifetime imaging (FLIM) was performed in TCSPC mode, using PicoHarp300 (PicoQuant) photon counting module. Pixel size was set to 70 nm, according to the Nyquist criterion. FLIM data were collected until 10,000 counts in the brightest pixel of an image. Data analysis and fitting were performed using SymphoTime64 using tail fit model with two exponential decay components (PicoQuant).

STochastic optical reconstruction microscopy (STORM)

Cells, fixed in 4% PFA, were treated with RNAse (Qiagen) at final concentration 1 mg/mL for 5 h at 37°C, washed with 1xPBS and stained with 2 nM YOYO (Thermo Scientific) solution dissolved in 1xPBS for 12–16 h at 4°C. Immediately prior to imaging, buffer solution in the samples was exchanged for GLOX buffer containing 0.5 mg/mL glucose oxidase (Sigma Aldrich), 40 μg/μL catalase (Sigma Aldrich), 10% glucose (Sigma Aldrich), 10% glycerol (Sigma Aldrich) and 1% β-mercaptoethanol in 1xPBS. Images

were acquired using Zeiss Spinning Disc confocal microscope (Zeiss) equipped with 100 x/1.46 oil objective, 488 nm diode laser and an Evolve 512 EMCCD camera (Photometrics). 6000 images per sample, with the seed of 5000 frames/s, were registered at 500 ms frame acquisition time. Single molecules were localized with ThunderSTORM plugin of ImageJ (650k – 800k per sample). Final images reconstructed with Voronoi tessellation to visualize local molecule density.

Light microscopy experiments were done at the Laboratory Of Imaging Tissue Structure And Function, core facility of Nencki Institute of Experimental Biology.

Structure illumination microscopy (SIM)

Fluorescence images were captured using LSM 780/ELYRA PS.1 (Zeiss) Structured Illumination Microscope (SIM), equipped with 63× PlanApo oil immersion objective (NA 1.4) and an iXon 885 EMCCD camera (Andor). Raw images (50 nm pixel size) were acquired at patterns 5 orientations, 5 phases, and processed into single optical sections with Zen 2012 (Zeiss, black edition).

SIM was performed in the Laboratory of Advanced Microscopy Techniques, core facility at Mossakowski Medical Research Centre, Polish Academy of Sciences.

Quantitative image analysis

Channels in the images were aligned using Zen software (Zeiss, Germany), using 0.5 μm fluorescent beads as the reference standard. All quantifications were performed using self-developed PartSeg Software (Bokota et al., 2021) in 3D images. Neuronal nuclei were distinguished based on NeuN neuronal marker staining and segmented based on DNA staining.

Chromatin was segmented by multi-thresholding using the Multiple Otsu algorithm (Liao et al., 2001), which separated the pixels of a 3D image into 7 classes according to the increasing gray levels intensity of the DNA staining within the image. Class 1 covered pixels with the minimal intensity values (interchromatin space and nucleoli), class 2 covered the most decondesed chromatin localized in the proximity to the interchromatin space, class 7 represented pixels with the highest pixel intensity values (the most condensed chromatin). The whole volume of chromatin was expressed as a percentage of nucleus volume and calculated based on the combined volume of classes 2–7. The coefficient of variation of the pixel brightness (CV) was calculated for DNA staining based on the ratio of the standard deviation of pixel brightness to the mean pixel brightness within the whole nucleus volume. Chromosomes 1 and 16, and nuclear speckles were segmented using the Multiscale Opening algorithm (Saha et al., 2017) and Maximal Entropy algorithm respectively.

RNA isolation

Total RNA was extracted using RNAeasy Mini Kit (Qiagen), according to the company's recommendations (a detailed protocol can be found on the producers website). Briefly, cells from the 6-well plates were disrupted in Buffer RLT and transferred to the RNAse-free tube. RNA was then purified on the spin column, including DNase I step, and eluted with 30 μL of nuclease-free water. Purity and concentration of RNA were measured using NanoDrop One (Thermo Scientific).

Transcriptomic analysis (RNA sequencing)

RNAseq libraries were prepared by KAPA Stranded mRNA Sample Preparation Kit according to the manufacturer's protocol (Kapa Biosystems, MA, USA) with modifications as described in Rajan et al. (Rajan et al., 2020). Transcriptomic data analysis was done as follows: fastq files were aligned to rn6 rat reference genome with STAR program (Dobin et al., 2013), reads were counted to genes using feature Counts algorithm (Liao et al., 2014). Gene counts were normalized with FPKM method and differential analysis was performed by DESeq2 (Love et al., 2014). Genes were considered to be differentially expressed (DE) with adjusted p value < 0.05. KEGG pathways analysis for DE genes was performed in R using clusterProfiler package (Yu et al., 2012).

Enrichment of up/down-regulated genes

To check for a significant enrichment/depletion of up- or down-regulated genes in certain chromosomes, random sampling procedure was applied to verify significance of enrichment or depletion of significantly changed genes. In details we sampled the same number of genes as the number of up- or down-regulated genes from the pool of all genes in the study (>32k genes) and verified how many of them are located in each chromosome. Sampling was repeated 1000 times to obtain a distribution of possible random assignments of genes to chromosomes. When the obtained number of our cLTP/CTRL up- or down-regulated genes was higher from 0.95, 0.99 or 0.999 quantile value from sampling experiment, it was assumed, that the probability of **enrichment** in certain chromosome was 95, 99, or 99.9% respectively and accordingly *, ** or *** assignments were given. On the other hand, when the obtained number of up- or down-regulated genes was lower than 0.05, 0.01 or 0.001 quantile value from sampling experiment, than it was assumed, that the probability of **depletion** in certain chromosome was 95, 99, or 99.9% respectively and accordingly *, ** or *** assignments were given.

cLTP/CTRL up -regulated genes clustering

To check whether up-regulated genes in cLTP/CTRL are distributed in closer proximity to each other, random selection of the same number of genes were sampled from all genes on chromosome 1 (4139 genes) and chromosomal distance (start site of second gene minus start site of first gene) was calculated for all pairs of neighboring genes. Assorted distribution of distances between two nearby

genes from shortest to longest for 1000 random selection of genes was compared to a distribution of distances of genes up-regulated in cLTP/CTRL.

Quantitative RT-PCR

One μg of total RNA was used in reverse transcription reaction with 10 μM deoxynucleotide triphosphates (Thermo Scientific), 1.25 μM of random hexamers (Eurx), 20 units of RiboLock RNase inhibitor (Thermo Scientific), and 100 units of SuperScript III Reverse Transcriptase (Invitrogen) in total volume of 20 μL. The cDNA synthesis was achieved by incubation at 25°C for 5 min followed by incubation at 50°C for 60 min. The qPCR reactions were performed using Power Up SYBR Green Master Mix (Applied Biosystems) with 2 ng of cDNA and 0.2 μM primers specific for HDAC1: forward –GCGAGCAAGATGGCGCAGACT, and reverse – GTGAGGCT TCATTGGGTGCCCT; and for the control genes GAPDH: forward – AGTTCAACGGCACAGTCAAG, reverse –TACTCAGCACCA GCATCACC or 18S rRNA forward – CCCAGTAAGTGCGGGTCATA, reverse – GGCCTCACTAAACCATCCAA. The primers were designed with Primer3 software (Koressaar and Remm, 2007; Untergasser et al., 2012). The qRT-PCR reactions and fluorescence measurements were performed using LightCycler ABI7300 Real-Time PCR system (Applied Biosystems), and the following parameters; 1) initial incubation at 50°C for 2 min for UDG activation, followed by denaturation at 95°C for 2 min, 2) 40 cycles of denaturation at 95°C for 15 s, annealing at 58°C for 15 s, and elongation at 72°C for 1 min. All sample analyses were performed in triplicates. Calculations were performed according to Livak et al.(Livak and Schmittgen, 2001). The CT for each sample was averaged and compared using the ΔΔCT method, where the amount of target RNA (ΔCT GOI) was normalized to either GADPH or 18S rRNA reference gene (ΔCT ref) and related to the amount of target gene in scrambled sample, which was set as the calibrator at 1.0.

QUANTIFICATION AND STATISTICAL ANALYSIS

All quantified data represent an average of at least triplicate samples. Statistical significance was determined using Prism 5.0. (GraphPad). $P < 0.05$ was considered significant (indicated by an asterisk in the figures), $P < 0.01$ (indicated by two asterisks in the figures), $P < 0.001$ (indicated by three asterisks in the figures).

Size of samples and statistical tests

Figure S1B and Figure 2B: CTRL: 10 min N = 286, 30 min N = 261, 60 min N = 255, 120 min N = 290, cLTP: 10 min N = 290, 30 min N = 291, 60 min N = 276, 120 min N = 279, Figure 2C: CTRL N = 24, cLTP N = 35. Statistical significance was determined by the two-tailed, unpaired Mann-Whitney test.

Figure S2 and Figure 3A: CTRL N = 187, for KCl 2h N = 130, Figure 3B: CTRL N = 50, for KA 2h N = 50, Figure 3C: CTRL N = 100, for FC 2h N = 56, Figure 3D: CTRL N = 100, for HFS 1h N = 200. Statistical significance was determined by the two-tailed, unpaired Mann-Whitney test.

Figure 4A: CTRL N = 204, cLTP N = 217, Figure 4B: CTRL N = 166, cLTP N = 222. Statistical significance was determined by the two-tailed, unpaired Mann-Whitney test.

Figure 5D: CTRL N = 142, cLTP N = 153. Statistical significance was determined by the two-tailed, unpaired Mann-Whitney test.

Figures S5F and 6C: for DRB treatment, CTRL N = 162, cLTP 2h N = 178, CTRL + INH N = 172, INH + cLTP 2h N = 111; for amanitin treatment CTRL N = 115, cLTP 2h N = 144, CTRL + INH N = 119, INH + cLTP 2h N = 127, Figure 6D: CTRL N = 119, cLTP 2h N = 114, CTRL + HEX N = 102, cLTP 2h + HEX N = 154, Figure 6E: CTRL N = 94, KCl 2h N = 66, CTRL + INH N = 108, INH + KCl 2h N = 94, Figure 6F: CTRL N = 132, cLTP 2h N = 129, CTRL + INH N = 133, INH + cLTP 2h N = 115, Figure 6G: CTRL N = 172, cLTP 2h N = 149, CTRL + INH N = 146, INH + cLTP 2h N = 137. Statistical significance was determined by the two-tailed, unpaired Kruskal-Wallis test.

Figure S7B and Figure 7D: SCR CTRL N = 82, SCR cLTP N = 70, ΔHDAC1 CTRL N = 64, ΔHDAC1 cLTP N = 58, Figure 7E: SCR CTRL N = 49, SCR cLTP N = 51, ΔHDAC1 CTRL N = 47, ΔHDAC1 cLTP N = 49

Figure S7C: SCR CTRL N = 102, SCR cLTP N = 114, ΔHDAC1 CTRL N = 134, ΔHDAC1 cLTP N = 100.